EMU Notes in Mineralogy, Vol. 21 (2024), Chapter 4, 57–110

Simple models for trace element fractionation during decompression melting of a two-lithology mantle

YAN LIANG

Department of Earth, Environmental and Planetary Sciences, Brown University, Providence, Rhode Island 02912, USA e-mail: yan_liang@brown.edu

Batch melting, fractional melting, continuous melting and two-porosity melting models have been used widely in geochemical studies of trace element fractionation during mantle melting. These simple melting models were developed for melting an homogeneous mantle source. Here we revisit and further develop these melting models in the context of decompression melting of a two-lithology mantle. Each lithology has its own source composition and melting parameters. During decompression melting, melt and solid flow vertically in the melting column. Part of the melt produced in one lithology is transferred to the other lithology at a prescribed rate. We use a set of conservation equations to solve for melt and solid mass fluxes, extent of melting and concentrations of a trace element in interstitial melt and aggregated melt in each lithology and mixed-column melt between the two lithologies. We uncover conditions under which batch melting, fractional melting, continuous melting and two-porosity melting models are realized during decompression melting through four case studies. We show that porosity in the continuous melting model varies along the melting column during decompression melting, contrary to what was assumed in its original development. We unify the batch melting, fractional melting, continuous melting and two-porosity melting models through a two-lithology melting model for decompression melting in a two-lithology mantle column. We discuss basic features of the two-lithology melting model through worked examples. We show that it is possible to produce partial and well-mixed melts with a range of REE patterns, from LREE depleted to LREE enriched, similar to those observed in mid-ocean ridge basalts by decompression melting of a two-lithology mantle.

1. Introduction

Models for trace element fractionation during mantle melting are essential to interpretation of basalts and peridotites. Simple models that have been used widely in geochemical studies of mantle melting include batch melting, fractional melting and continuous melting models (*e.g.* Shaw, 2006; Zou, 2007 and references therein). The continuous melting model is also referred to as the dynamic melting model in the literature (*e.g.* McKenzie, 1985; Albarède, 1995; Zou, 1998; Shaw, 2000). These simple melting models were originally developed by considering mass balance for a mantle parcel, irrespective of flows of partial melt and residual solid in the melting region (*e.g.* Gast, 1968; Shaw, 1970, Langmuir *et al.*, 1977; McKenzie, 1985; Albarède, 1995; Zou, 1998; Shaw, 2000). It has been shown in subsequent studies that these simple melting models can also be derived by considering flows of melt and solid in an upwelling steady-state melting column (*e.g.* Ribe, 1985; Spiegelman and Elliott, 1993; Iwamori, 1994; Asimow and

DOI: 10.1180/EMU-notes.21.4

Stolper, 1999; Lundstrom, 2000; Liang, 2008; Liang and Peng, 2010). During batch melting, both partial melt and residual solid flow upwards in the melting column and no melt is extracted to melt conduits or high-porosity channels along the melting column (*e.g.* Ribe, 1985; Spiegelman and Elliott, 1993; Asimow and Stolper, 1999). During fractional melting, melt generated at any point in the melting column is completely and instantaneously removed from the residual solid. The melt fraction or porosity is zero in the residuum. During continuous or dynamic melting, a small but constant fraction of melt (typically $<2\%$) is retained in the residuum after an initial stage of batch melting (Langmuir *et al.*, 1977; McKenzie, 1985; Albarède, 1995; Zou, 1998; Shaw, 2000). In a physically more realistic setting, only a fraction of melt is extracted through high-porosity channels and the remaining melts percolate through the melting column. Consequently, the porosity increases upwards in the melting column (*e.g.* Ribe, 1985; Hewitt and Fowler, 2008; Liang and Liu, 2018). This leads to the two-porosity melting models (*e.g.* Iwamori, 1994; Lundstrom, 2000; Ozawa, 2001; Jull *et al.*, 2002; Liang and Parmentier, 2010; Liang and Peng, 2010). In this chapter, we will take a closer look at these simple melting models from a standpoint of mass conservation of the melt and residual solid in an upwelling steady-state melting column.

The batch, fractional, continuous and two-porosity melting models were originally developed for modelling trace element variations during partial melting of a homogeneous mantle source. There is growing evidence that the source region for mantle-derived magmas is chemically (depleted *vs.* enriched) and lithologically (peridotite *vs.* pyroxenite) heterogeneous. The heterogeneities are long lived and probably produced by tectonic processes involving crustal formation, crust and mantle recycling and core-mantle interaction (*e.g.* Zindler and Hart, 1986; Hofmann, 1997; Stracke, 2012; White, 2015). There are several types of heterogeneities in the mantle. In terms of radiogenic isotope ratios, the mantle source is identified as the depleted mantle and the enriched mantle of various types (*e.g.* EM I, EM II, HIMU, FOZO, Zindler and Hart, 1986; Hofmann, 2003). The lithology of the depleted mantle is generally ascribed to lherzolite and its composition is relatively well constrained (*e.g.* Salters and Stracke, 2004; Workman and Hart, 2005). Compositions of enriched mantle components are model dependent as they are estimated by mixing the depleted mantle with various proportions of the recycled or subducted oceanic crust, ancient pelagic or terrigenous sediments and/or lower continental crust (*e.g.* Weaver, 1991; Stracke *et al.*, 2003; Willbold and Stracke, 2006; Turner *et al.*, 2017). The lithology of the enriched mantle could be pyroxenite, eclogite, or peridotite. One important petrological observation is that the solidi of garnet pyroxenite, eclogite and carbonated peridotite are lower than the solidus of anhydrous lherzolite (*e.g.* Yasuda *et al.*, 1994; Pertermann and Hirschmann, 2003; Kogiso *et al.*, 2004; Dasgupta *et al.*, 2006; Lambart *et al.*, 2016). During decompression melting of a veined mantle, garnet pyroxenite and eclogite melt at greater depth than their surrounding peridotites. Melts derived from the garnet pyroxenite and eclogite react with their surrounding peridotites, producing secondary pyroxenites that are enriched in orthopyroxene (Opx) or clinopyroxene (Cpx) (*e.g.* Yaxley and Green, 1998; Lo Cascio, 2008; Lambart *et al.*, 2012; Mallik and Dasgupta, 2012; Wang *et al.*, 2013, 2020; Borghini *et al.*, 2017, 2020; Soderman *et al.*, 2022). One of the objectives of this study is to expand the existing melting models so we can include a second lithology in an upwelling melting column.

To model trace element fractionation during partial melting of a heterogeneous mantle source, the standard geochemical treatment is melting followed by mixing (*e.g.* Vollmer, 1976; Langmuir *et al*., 1978). In this two-step approach, one first uses one of the simple melting models to calculate compositions of melt derived from the depleted mantle source and the enriched mantle source in two independent calculations. One then mixes the two melts in different proportions to obtain a set of mixed melt compositions and compares the modelling results with geochemical observations. This melting followed by mixing approach has been used widely in the interpretation of trace element and isotope data of oceanic basalts (*e.g.* Langmuir *et al*., 1978; Zindler *et al*., 1984; Niu *et al*., 2002; Ito and Mahoney, 2005; Stracke and Bourdon, 2009; Rudge *et al*., 2013; Shimizu *et al*., 2016; Shorttle *et al*., 2016). As the two melting calculations are independent of each other, there is no mass transfer between the enriched and depleted mantle in the melting region. Mixing takes place at the top of the melting region.

The purpose of this chapter is to present the batch, fractional, continuous and two-porosity melting models in the context of decompression melting of an upwelling two-lithology melting column in which melts produced in one lithology flow into and interact with the melt and residual solid in another lithology. The presence of the second lithology also allows us to model the formation of high-porosity channels, a process that has not been considered in the two-porosity melting models (*e.g.* Iwamori, 1994; Lundstrom, 2000; Ozawa, 2001; Jull *et al*., 2002; Liang and Peng, 2010; but see Liang and Parmentier, 2010). Here we consider a set of general problems in which the mantle source consisted of two lithologies: A and B. Figure 1 presents a simplified treatment in which the background lithology A has a larger volume fraction in the melting region. To obtain steady-state solutions, we assume that the shape of lithology B is in the form of long strings (Fig. 1a). We subdivide the melting region into vertical columns; each contains a pair of A-B. For a given melting column (Fig. 1b), the two lithologies have their own volume fractions (ψ_A, ψ_B), source compositions (C_A^0, C_B^0), melting rates (Γ_A, Γ_B), degrees of melting (F_A, F_B), porosities (ϕ_f^A, ϕ_f^B), melting reactions and bulk solid-melt partition coefficients for the trace element of interest (k_A, k_B). In the lowest part of the melting column ($F_A \le F_A^d$), melt fractions are small. There is no lateral melt flow across the lithological boundary and batch melting prevails in the two lithologies. As there is no chemical interaction between the two lithologies, the models presented in this study are also applicable to cases when the depth for the onset of melting for one lithology is different from another lithology. In the upper part of the melting column ($F_A > F_A^d$), part of the melt generated in lithology A at a given location in the melting column (*e.g.* z_1 in Fig. 1b) is transferred laterally into lithology B where it mixes locally with the melt produced in lithology B. The mixed melt percolates and re-equilibrates with the residual solid in lithology B in the overlying melting column. The amount of melt flowing from lithology A to lithology B per unit volume of the two lithologies per unit time is called the melt suction rate ($\dot{S}$), a key parameter in the models presented in this study. At the top of the melting column, melts from lithology A and lithology B mix with each other, forming the mixed-column melt for the two-lithology melting column.

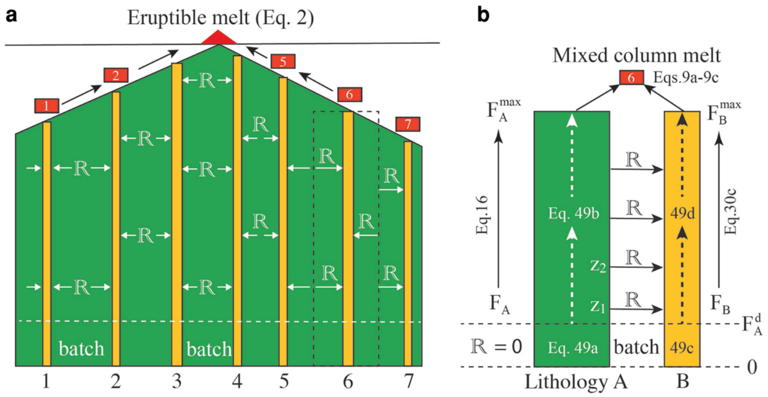

Fig. 1. (***a***) Schematic diagram showing an upwelling melting region that consists of two lithologies, A (green) and B (orange). Lithology B has a smaller volume fraction and is in the form of long vertical strings (labelled 1, 2, …, 7). (***b***) Mass transfer in an idealized two-lithology melting column (equivalent to dashed box in panel a). The lower part of the melting column ($F_A \le F_A^d$) experiences batch melting during which melts generated in the two lithologies do not interact with each other. The melt suction rate is zero. Part of the melt generated in lithology A in the upper part of the melting column ($F_A > F_A^d$) is transferred to lithology B at a prescribed melt suction rate of $\mathbb{R}$ (Eq. 17c). Mixing of melts from lithology A and lithology B at top of the melting column produces the mixed-column melt (boxes 1 to 7). The eruptible melt is formed by pooling mixed-column melts from columns 1, 2, …, 7 in prescribed proportions. Key equations for concentrations of a trace element in the interstitial melt in the two lithologies, mixed-column melt at top of the melting column, and eruptible melt over the melting region are identified (Eqs. 9a–9c, 49a–49d and 2).

Finally, the mixed-column melts from selected melting columns aggregate and mix with each other across the melting region (*e.g.* columns 5, 6 and 7 in Fig. 1a), forming the eruptible melt. Although highly simplified, the scenario outlined here is broadly consistent with the process of high-porosity harzburgite and dunite channel formation in an upwelling mantle column (*e.g.* Liang *et al.*, 2010; Schiemenz *et al.*, 2011) and melt transport along decompaction channels at top of the melting region (*e.g.* Sparks and Parmentier, 1991). The flux of percolating melt must be high enough to form high-porosity channels in the upwelling column. This is achieved by the initial batch melting in the lowest part of the melting region and by the higher melting or/and dissolution rate of the enriched lithology.

Our main objective is to obtain simple mathematical expressions for concentrations of a trace element in interstitial melts and residual solids in lithology A and lithology B in the melting column, concentration of the trace element in the mixed-column melt collected at top of the melting column and concentration of the eruptible melt pooled across the melting region. In an upwelling melting column where melt and solid flow at different velocities, it is necessary to keep track of spatial variations of the melt and solid in the melting column. This is done through applications of mass conservation equations. Here we show how the conservation equations can be used to construct simple melting models and to understand their physical meanings. Appendices A and B present two sets of conservation equations for modelling trace element fractionation in lithology A and lithology B during concurrent melting and melt migration in a one-dimensional (1D) melting column. To connect to the batch, fractional, continuous and two-porosity melting models, we consider four steady-state problems in which concentrations, velocities and volume fractions of the melt and solid vary as a function of location in the melting column but are independent of time. For simplicity, we assume that the melting rate and volume fraction of each lithology are constant and uniform in the melting column and that the melt suction rate takes on one or two constant values. Following previous treatment, we assume that residual solid and interstitial melt are in local chemical equilibrium in each of the two lithologies. These simplifications allow us to obtain simple analytical solutions to the two-lithology melting problems and to gain new insights into the geochemical consequence of decompression melting of a two-lithology mantle.

Here, detailed step-by-step derivations of the four melting models are presented in sections 3–5. For the convenience of geochemical modelling, the main equations for each of the melting models in Appendix E are summarized. To set up the study in sections 3–5, simple derivations for the composition of mixed-column melt at top of the two-lithology melting column (C_f^{mix}) and the composition of eruptible melt pooled from several melting columns in the melting region ($C_f^{eruptible}$) are presented first. Mathematical expressions for these mixed-melt compositions are general and independent of assumptions of the underlining melting models (Appendix C). Figure 2 is a roadmap that outlines the relationships among the melting models presented in this study. For modelling trace element fractionation during decompression melting of a heterogeneous mantle, the more general two-lithology melting model which reduces to the batch melting, fractional melting, continuous melting and two-porosity melting models under special conditions is recommended.

2. Compositions of mixed-column melt and eruptible melt

2.1. Compositions of the eruptible melt and the overall average melt

If we pool all the melts collected at the top of each melting column, we obtain the average melt for the entire melting region. Let $C_{f,j}^{mix}$ be the concentration of a trace element of interest in the mixed-column melt derived from lithology A and lithology B at the top of column j and $\bar{F}_j$ be the average degree of melting for the two-lithology melting column j. The overall average melt composition (C_f^{avg}) is the weighted mean of mixed-column melts from all the melting columns, *i.e.*

$$C_f^{avg} = \frac{\bar{F}_1 C_{f,1}^{mix} + \bar{F}_2 C_{f,2}^{mix} + \ldots + \bar{F}_N C_{f,N}^{mix}}{\bar{F}_1 + \bar{F}_2 + \ldots + \bar{F}_N} \tag{1a}$$

$$\bar{F}_j = \psi_{A,j} F_{A,j} + \psi_{B,j} F_{B,j} \tag{1b}$$

$$\psi_{A,j} + \psi_{B,j} = 1 \tag{1c}$$

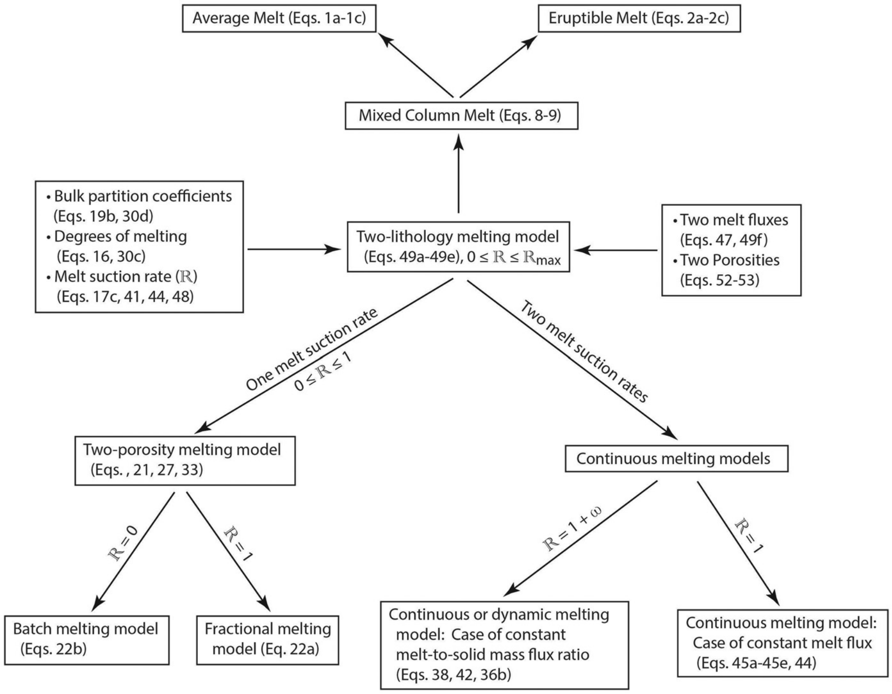

Fig. 2. Roadmap illustrating relationships among the various melting models presented here. The two-lithology melting model is the most general. It has three sets of melting parameters, two melt fluxes and two porosities. Depending on the choice of melt suction rate, the two-lithology melting model is reduced to the batch melting, fractional melting, continuous melting, and two-porosity melting models under specified limits. The mixed column melt is a mixture of melts derived from lithology A and lithology B at top of the melting column. The eruptible melt is formed by pooling mixed-column melts from different melting columns. The average melt is the weighted mean of all the melts collected at top of each melting column. Key equations are identified in the figure and summarized in Appendix E.

where N is the number of two-lithology melting columns in the melting region ($N = 7$ in Fig. 1a); and subscript j (=1, 2, …, N) refers to properties of lithology A or lithology B of column j. For example, $\psi_{A,j}$ is the volume fraction of lithology A in column j. The volume fractions of A and B in one melting column can be different from those in another melting column. Key symbols used in this note are listed in Table 1.

If mixing of melts from different melting columns is incomplete, the composition of mixed melt would depend on the amount of melt contributed from each melting column. A collection of incompletely mixed melts from different melting columns is referred to as the eruptible melt, the composition of which is given by the general expression:

$$C_f^{eruptible} = \alpha_1 C_{f,1}^{mix} + \alpha_2 C_{f,2}^{mix} + \ldots + \alpha_N C_{f,N}^{mix} \tag{2a}$$

Table 1. List of key symbols.

Symbol	Description
C_A^0, C_B^0	Concentration of the bulk solid A or B at the onset of melting
C_f^A, C_f^B	Concentration of a trace element in interstitial melt in lithology A or B
C_f^{avg}	Concentration of the average melt for the entire melting region
$C_f^{mix}, C_{f,j}^{mix}$	Concentration of the mixed-column melt for column j
$\bar{C}_f^A$	Average concentration of melts sucked from lithology A to lithology B
C_s^A, C_s^B	Concentration of a trace element in residual solid in lithology A or B
d_A, d_B	Mean grain size of lithology A or lithology B
F_A, F_B	Degree of melting experienced by lithology A or lithology B
$F_A^{\max}, F_B^{\max}$	Maximum extent of melting at top of the melting column
F_d^A, F_d^B	Maximum extent of batch melting in the lower part of the melting column
$\bar{F}_j$	Average degree of melting for the two-lithology melting column j
k_A^0, k_B^0	Bulk partition coefficient at the onset of melting for lithology A or B
k_A^p, k_B^p	Bulk partition coefficient according to the melting reaction of A or B
k_A, k_B	Bulk solid-melt partition coefficient for lithology A or lithology B
n	Porosity exponent in the permeability model
p_j^A, p_j^B	Modal proportion of mineral j in the melting reaction of lithology A or B
$\mathbb{R}$	Dimensionless melt suction rate
$\dot{S}$	The rate of melt extracted from lithology A to lithology B
V_f^A, V_f^B	Velocity of the interstitial melt in lithology A or lithology B
V_s^A, V_s^B	Velocity of the solid in lithology A or lithology B in the melting column
V_s^0	Solid upwelling rate at the onset of melting
w_j^A, w_j^B	Modal proportion of mineral j in lithology A or lithology B
z	Vertical coordinate with origin at the bottom of the melting column
α_j	Fraction of contribution to the eruptible melt from column j
ϕ_f^A, ϕ_f^B	Porosity of lithology A or lithology B
$\phi_{ref}^A, \phi_{ref}^B$	Reference porosity of lithology A or lithology B
$\kappa_\phi^A, \kappa_\phi^B$	Permeability of lithology A or lithology B
ω	Ratio of melt-to-solid mass flux for the continuous melting model
$\Gamma_A,\ \Gamma_B$	Melting rate of lithology A or lithology B
$\rho_f,\ \rho_s$	Density of the melt or solid
ψ_A, ψ_B	Volume fraction of lithology A or lithology B

$$\alpha_1 + \alpha_2 + \ldots + \alpha_N = 1 \quad \text{and} \quad 0 \le \alpha_j \le 1 \tag{2b}$$

where the weighing factor α_j is model dependent. The weighing factor is zero for columns that do not contribute to the eruptible melt. Equation 2a is reduced to Eq. 1a when the weighing factor is proportional to the volume or volume flux of melt produced from each of the two-lithology melting columns, *i.e.*

$$\alpha_j = \frac{\bar{F}_j}{\bar{F}_1 + \bar{F}_2 + \ldots + \bar{F}_N} \tag{2c}$$

The mixing proportion (α_j) is determined by a mixing mechanism which is not well constrained. Rudge *et al.* (2013) proposed a statistical model for calculating the weighing factor in Eq. 2a for the eruptible melt produced by fractional melting of a two-lithology mantle. Shimizu *et al.* (2016) and Shorttle *et al.* (2016) used this model to study variations in trace elements and Nd isotope ratio in MORB samples. Liu and Liang (2020) studied the effect of incomplete mixing on Sr-Nd-Hf-Pb isotope ratios and incompatible trace element abundances in pooled melts collected at top of a triangular melting region by setting the weighing factor in Eq. 2a to zero for selected melting columns. Liang (2022) used Eq. 1a-1c and a mixing scheme to model along ridge variations in Sr-Nd-Hf isotope ratios in pooled melts produced by fractional melting of a two-lithology mantle. These studies have demonstrated the importance of incomplete mixing in producing large variations in radiogenic isotope ratios and highly incompatible trace element abundances in oceanic basalts. However, a process-based mixing model still awaits future developmemt, a topic that is beyond the scope of this chapter.

In the next section, general expressions for the concentration of a trace element in the well mixed-column melt for the two-lithology melting column j are presented. To simplify notations, we drop the subscript j for all the variables for column j in the equations presented in the remainder of this chapter.

2.2. Composition of the mixed-column melt

Let's start with the classic problem of batch melting in a closed box. As no mass has entered or left the box, concentrations of a trace element in the melt (C_f) and residual solid (C_s) are related to each other through the mass balance equation:

$$FC_f + (1-F)C_s = C_s^0 \tag{3}$$

where F is the fraction of melt in the system and C_s^0 is the solid concentration before melting. If the melt and residual solid are in chemical equilibrium, we obtain the batch melting model:

$$C_f = \frac{C_s^0}{k + (1-k)F} \tag{4}$$

where k is the bulk solid-melt partition coefficient. Let us now expand this exercise by considering batch melting of lithology A and lithology B in the same box. The two lithologies are isolated from each other except at top of the melting column where melts derived from the two lithologies mix completely with each other, forming the well mixed-column melt. Applying Eq. 3 to lithology A and lithology B, respectively, we have:

$$F_A C_f^A + (1 - F_A) C_s^A = C_A^0 \tag{5a}$$

$$F_B C_f^B + (1 - F_B) C_s^B = C_B^0 \tag{5b}$$

where superscripts A and B refer to properties of lithology A and lithology B, respectively. Taking a weighted sum of Eqs 5a and 5b, we have:

$$\psi_A \left[F_A C_f^A + (1 - F_A) C_s^A \right] + \psi_B \left[F_B C_f^B + (1 - F_B) C_s^B \right] = \psi_A C_A^0 + \psi_B C_B^0 \tag{6}$$

where ψ_A and ψ_B are volume fractions of A and B in the melting column. Rearranging Eq. 6, we have:

$$\psi_A F_A C_f^A + \psi_B F_B C_f^B = \psi_A \left[C_A^0 - (1 - F_A) C_s^A \right] + \psi_B \left[C_B^0 - (1 - F_B) C_s^B \right] \tag{7}$$

The mixed-column melt concentration is the weighted average of melts from lithologies A and B, *i.e.*

$$C_f^{mix} = \frac{\psi_A F_A C_f^A + \psi_B F_B C_f^B}{\psi_A F_A + \psi_B F_B} \tag{8}$$

The denominator in Eq. 8 is the average degree of melting of the two-lithology melting column. Substituting Eq. 7 into Eq. 8, we have an alternative expression for the mixed-column melt concentration:

$$C_f^{mix} = \frac{\psi_A \left[C_A^0 - (1 - F_A) C_s^A \right] + \psi_B \left[C_B^0 - (1 - F_B) C_s^B \right]}{\psi_A F_A + \psi_B F_B} \tag{9a}$$

which can also be written in terms of concentrations of interstitial melts in lithologies A and B:

$$C_f^{mix} = \frac{\psi_A \left[C_A^0 - (1 - F_A) k_A C_f^A \right] + \psi_B \left[C_B^0 - (1 - F_B) k_B C_f^B \right]}{\psi_A F_A + \psi_B F_B} \tag{9b}$$

For non-modal melting during which the bulk partition coefficient varies as a function of the degree of melting, we have:

$$C_f^{mix} = \frac{\psi_A\left[C_A^0 - \left(k_A^0 - k_A^p F_A\right)C_f^A\right] + \psi_B\left[C_B^0 - \left(k_B^0 - k_B^p F_B\right)C_f^B\right]}{\psi_A F_A + \psi_B F_B} \tag{9c}$$

where k^0 is the bulk solid-melt partition coefficient at the onset of melting; and k^p is the bulk solid-melt partition coefficient according to melting reaction for lithology A or lithology B (see Eqs 18–19 below). The differences in the two square brackets on the right-hand-side of Eqs 9a–9c are the amount of melt produced by melting of lithology A and lithology B, respectively. In Appendix C, we show that Eqs 8 and 9 are general expressions for the concentration of mixed-column melt produced by decompression melting of a two-lithology mantle, irrespective of how the two lithologies interact in the melting column. These equations highlight the importance of composition and volume proportion of the mantle source and extent of melting in geochemical mixing calculations.

For highly incompatible trace elements, their concentrations in residual solids become negligible after a small to moderate extent of melting. Equation 9a can be simplified as:

$$C_f^{mix} \approx \frac{\psi_A C_A^0 + \psi_B C_B^0}{\psi_A F_A + \psi_B F_B} \tag{10a}$$

Hence mixing of melts from lithology A and lithology B at top of the melting column is equivalent to mixing of the two sources weighted by the fraction of melts produced in the two-lithology column. As the demonimator in Eq. 10a is generally less than one, the concentration of the mixed melt is greater than the concentration of the mixed-mantle source. The demonimator in Eq. 10a is cancelled out when taking a ratio of two highly incompatible trace elements or two isotopes of the same element. For ^{87}Sr/^{86}Sr, we have

$$\frac{^{87}C_f^{mix}}{^{86}C_f^{mix}} \approx \frac{\psi_A {}^{87}C_A^0 + \psi_B {}^{87}C_B^0}{\psi_A {}^{86}C_A^0 + \psi_B {}^{86}C_B^0} \tag{10b}$$

In terms of isotope or element ratios of highly incompatible trace elements, mixing of melts from lithology A and lithology B at top of the melting column is equivalent to mixing of the two sources. Hence one cannot distinguish source mixing from magma mixing using highly incompatible trace elements unless the extent of melting is very small. This statement is independent of melting models.

For moderately incompatible and compatible trace elements, the mixed-column melt composition depends on melt or residual solid compositions at top of the melting column, hence the melting models. In the next three sections, we present two classes of melting models, one has a constant and uniform melt suction rate (section 3) and the other has two melt suction rates (sections 4–5). We show how these melting models are related to the batch, fractional, continuous and two-porosity melting models. In section 6, we take a closer look at the various melting models by comparing porosities derived from the melting models. Finally in section 7, we present examples of calculated melt compsitions using the two-lithology melting model.

3. Case of constant and uniform melt suction rate

First, a simple case in which the melt suction rate is constant and uniform in the melting column is considered. This case was first examined by Iwamori (1994) for mantle melting with diffuse and channelized porous flow. The melting region is treated as two overlapping continua consisting of low-porosity matrix (lithology A) and interconnected high-porosity channels (lithology B). However, the process of high-porosity channel formation was not considered in this class of two-porosity melting models (*e.g.* Iwamori, 1994; Lundstrom, 2000; Ozawa, 2001; Jull *et al.*, 2002; Liang, 2008; Liang and Peng, 2010). Here we complete this model by explicitly modelling high-porosity channel formation in lithology B. Section E1 in Appendix E summarizes the main results. Below we provide a detailed derivation.

3.1. Trace element concentrations in lithology A

We start with the steady-state mass conservation equation for concentration of a trace element in interstitial melt in lithology A in the 1D melting column:

$$\left[\rho_f \phi_f^A V_f^A + \rho_s\left(1-\phi_f^A\right)V_s^A k_A\right]\frac{dC_f^A}{dz} = \left(k_A^p - 1\right)C_f^A \Gamma_A \tag{11a}$$

where ρ_f and ρ_s are densities of the melt and solid, respectively; ϕ_f^A and V_f^A are the porosity and velocity of interstitial melt in the melting column; V_s^A is the residual solid velocity; k_A^p is the bulk solid-melt partition coefficient according to melting reaction (Eq. A9 in Appendix A); and z is the vertical coordinate, positive upwards. For convenience, we set the origin of our coordinate system ($z = 0$) to the solidus of lithology A (Fig. 1b). At the solidus, concentration of the melt is related to concentration of the mantle source of A (C_A^0) via equilibrium partitioning:

$$C_f^A(0) = \frac{C_A^0}{k_A^0} \tag{11b}$$

where k_A^0 is the bulk solid-melt partition coefficient at the onset of melting.

To solve the melt concentration from Eqs 11a and 11b, we need to know how mass fluxes of the melt, $\rho_f \phi_f^A V_f^A$ and solid, $\rho_s\left(1-\phi_f^A\right)V_s^A$ vary spatially in the melting column. This is an important feature of steady-state melting: concentration of a trace element in the melt depends on the product of volume fraction and velocity of the melt and solid, respectively, not their individual values. The mass fluxes can be calculated using the steady-state mass conservation equations for the interstitial melt and residual solid in lithology A. From Eqs A1 and A2, we have:

$$\frac{d\rho_f \phi_f^A V_f^A \psi_A}{dz} = \psi_A \Gamma_A - \dot{S} \tag{12a}$$

$$\frac{d\rho_s \left(1 - \phi_f^A\right) V_s^A \psi_A}{dz} = -\psi_A \Gamma_A \tag{12b}$$

At the solidus ($z = 0$), melt fraction is zero and solid velocity equals to the upwelling velocity of the mantle source (V_s^0). Integrating Eqs 12a and 12b for constant melting rate and melt suction rate, we have:

$$\rho_f \phi_f^A V_f^A = \left(\Gamma_A - \frac{\dot{S}}{\psi_A}\right) z \tag{13a}$$

$$\rho_s \left(1 - \phi_f^A\right) V_s^A = \rho_s V_s^0 - \Gamma_A z \tag{13b}$$

In response to melting and melt extraction, the mass flux of the melt increases upwards in the melting column. This is an important feature of the constant melt suction rate model.

In geochemical studies, it is common practice to express melt and solid concentrations as a function of the extent of melting experienced by residual solid. The evolution equation relating the degree of melting (F_A) to melting rate (Γ_A) is Eq. A6 in Appendix A. At steady state, we have:

$$V_s^A \frac{dF_A}{dz} = \frac{(1 - F_A)\Gamma_A}{\rho_s \left(1 - \phi_f^A\right)} \tag{14}$$

Substituting Eq. 13b into Eq. 14, we have

$$\frac{dF_A}{dz} = \frac{(1 - F_A)\Gamma_A}{\rho_s V_s^0 - \Gamma_A z} \tag{15}$$

Integrating Eq. 15 from solidus ($z = 0$, $F_A = 0$), we obtain the degree of melting for lithology A:

$$F_A = \frac{1}{\rho_s V_s^0} \int_0^z \Gamma_A dz = \frac{\Gamma_A z}{\rho_s V_s^0} \tag{16}$$

Hence for constant melting rate, the degree of melting increases linearly as a function of z in the melting column. For variable melting rate, we use the integral version of Eq. 16 to calculate the degree of melting. In terms of the degree of melting, the mass fluxes of the melt and solid in Eqs 13a and 13b take on the expressions (Iwamori, 1994; Lundstrom, 2000; Jull *et al*., 2002; Liang and Peng, 2010):

$$\rho_f \phi_f^A V_f^A = \rho_s V_s^0 (1-\mathbb{R}) F_A \tag{17a}$$

$$\rho_s \left(1-\phi_f^A\right) V_s^A = \rho_s V_s^0 (1-F_A) \tag{17b}$$

where $\mathbb{R}$ is the dimensionless melt suction rate, defined as

$$\mathbb{R} = \frac{\dot{S}}{\psi_A \Gamma_A} \tag{17c}$$

For the problem considered here $0 \le \mathbb{R} \le 1$.

Finally, during mantle melting, mineral modes in the residuum change according to the melting reaction. The bulk solid-melt partition coefficient varies as a function of extent of melting experienced by the solid. We can use the following steady-state equation to calculate spatial variations of the bulk partition coefficient in the melting column (see also Eq. A7):

$$V_s^A \frac{dk_A}{dz} = \frac{\left(k_A - k_A^p\right)\Gamma_A}{\rho_s\left(1-\phi_f^A\right)} \tag{18a}$$

Substituting the solid mass flux (Eq. 13b) into Eq. 18a, we have:

$$\frac{dk_A}{dz} = \frac{\left(k_A - k_A^p\right)\Gamma_A}{\rho_s V_s^0 - \Gamma_A z} \tag{18b}$$

For constant k_A^p, we have:

$$\frac{k_A - k_A^p}{k_A^0 - k_A^p} = \frac{\rho_s V_s^0 - \Gamma_A z}{\rho_s V_s^0} = 1 - \frac{\Gamma_A z}{\rho_s V_s^0} \tag{19a}$$

which can also be written in terms of the degree of melting experienced by lithology A:

$$k_A = \frac{k_A^0 - k_A^p F_A}{1 - F_A} \tag{19b}$$

Equation 19b is the familiar expression relating bulk partition coefficient to degree of melting and partition coefficients for the melting reaction and at the onset of melting (*e.g.* Shaw, 1970).

We can now calculate the interstitial melt composition by substituting Eqs 16, 17 and 19b into Eq. 11a which takes on the form:

$$\frac{dC_f^A}{dF_A} = \frac{\left(k_A^p - 1\right)C_f^A}{k_A^0 + \left(1 - k_A^p - \mathbb{R}\right)F_A} \tag{20}$$

When $1 - k_A^p - \mathbb{R} \neq 0$, we have an expression for the interstitial melt composition:

$$C_f^A = \frac{C_A^0}{k_A^0}\left[\frac{k_A^0 + \left(1 - k_A^p - \mathbb{R}\right)F_A}{k_A^0}\right]^{\frac{k_A^p - 1}{1 - k_A^p - \mathbb{R}}} \tag{21a}$$

When $1 - k_A^p - \mathbb{R} = 0$, we have:

$$C_f^A = \frac{C_A^0}{k_A^0}\exp\left(\frac{k_A^p - 1}{k_A^0}F_A\right) \tag{21b}$$

Equation 21a was first obtained by Iwamori (1994). Equation 21b is a special case that arises from integration of Eq. 20. There are two physical parameters in this model: degree of melting experienced by lithology A (F_A) and dimensionless melt suction rate ($\mathbb{R}$). When $\mathbb{R} = 1$, all the melt produced in lithology A is sucked into lithology B along the melting column. The vertical melt flux, hence porosity, reduces to zero in lithology A (Eq. 17a). Equation 21a reduces to the non-modal perfect fractional melting model of Shaw (1970), *i.e.*

$$C_f^A = \frac{C_A^0}{k_A^0}\left(1 - \frac{k_A^p}{k_A^0}F_A\right)^{\frac{1 - k_A^p}{k_A^p}} \tag{22a}$$

When $\mathbb{R} = 0$, no melt produced in lithology A is transferred into lithology B. Equation 21a reduces to the non-modal batch melting model, i.e.

$$C_f^A = \frac{C_A^0}{k_A^0 + \left(1 - k_A^p\right)F_A} \tag{22b}$$

Hence batch and perfect fractional melting models are special cases of the steady-state melting model with a constant and uniform melt suction rate. Given the melt composition, concentration of the trace element in the residual solid or minerals can be calculated using solid-melt or mineral-melt partition coefficients. For the residual solid, we have:

$$C_s^A = k_A C_f^A \tag{23}$$

3.2. Average concentration of a trace element in lithology A

The average concentration of a trace element in melts sucked from lithology A to lithology B is a collection of transferred melts along the melting column, *i.e.*

$$
\begin{aligned}
\bar{C}_f^A &= \frac{1}{\mathbb{R}F_A}\int_0^{F_A} \mathbb{R}C_f^A dF_A \\
&= \frac{C_A^0}{\mathbb{R}F_A}\left\{1-\left[\frac{k_A^0+\left(1-k_m^p-\mathbb{R}\right)F_A}{k_A^0}\right]^{\frac{-\mathbb{R}}{1-k_m^p-\mathbb{R}}}\right\}
\end{aligned}
\qquad (24)
$$

Equation 24 is valid for $\mathbb{R} > 0$. When $\mathbb{R} = 0$, the average melt is undefined as no melt is transferred from lithology A to lithology B. To gain additional insights into the average melt composition, we seek an alternative expression for the average melt composition using the conserved form of the mass conservation equation for lithology A (Eq. A3). The steady-state version of Eq. A3 is:

$$
\frac{d\left[\rho_f\phi_f^A V_f^A C_f^A+\rho_s\left(1-\phi_f^A\right)V_s^A C_s^A\right]}{dz} = -\frac{\dot{S}}{\psi_A}C_f^A \qquad (25)
$$

Replacing the melt and solid mass fluxes and spatial coordinate in Eq. 25 by the degree of melting via Eqs 16–17, we have an ordinary differential equation with variable F_A:

$$
\frac{d\left[(1-\mathbb{R})F_A C_f^A+(1-F_A)C_s^A\right]}{dF_A} = -\mathbb{R}C_f^A \qquad (26)
$$

Integrating both sides of Eq. 26 from the solidus, we have:

$$
\bar{C}_f^A = \frac{C_A^0-\left[(1-\mathbb{R})F_A C_f^A+(1-F_A)C_s^A\right]}{\mathbb{R}F_A} \qquad (27a)
$$

where values of C_f^A and C_s^A correspond to the extent of melting F_A. When the solid and melt are in local chemcial equilibrium, we have:

$$
\bar{C}_f^A = \frac{C_A^0-[(1-\mathbb{R})F_A+(1-F_A)k_A]C_f^A}{\mathbb{R}F_A} \qquad (27b)
$$

The physical meaning of Eq. 27 becomes clear after the rearrangment:

$$
C_A^0 = (1-\mathbb{R})F_A C_f^A+(1-F_A)C_s^A+\mathbb{R}F_A\bar{C}_f^A \qquad (28a)
$$

Multiplying both sides of Eq. 28a by the total mass flux of lithology A, we have an overall mass flux balance equation for the trace element in lithology A:

$$\rho_s V_s^0 C_A^0 = \rho_s V_s^0 (1-\mathbb{R}) F_A C_f^A + \rho_s V_s^0 (1-F_A) C_s^A + \rho_s V_s^0 \mathbb{R} F_A \bar{C}_f^A \tag{28b}$$

In terms of melt production, Eq. 28b can also be written as:

$$\rho_s V_s^0 (1-\mathbb{R}) F_A C_f^A + \rho_s V_s^0 \mathbb{R} F_A \bar{C}_f^A = \rho_s V_s^0 C_A^0 - \rho_s V_s^0 (1-F_A) C_s^A \tag{28c}$$

Equation 28b states that the total mass flux of the trace element in lithology A feeding into the melting column from below equals to the sum of mass fluxes of the trace element in interstitial melt and residual solid at a given location or F_A in the melting column (first two terms on the right hand side) and the total mass flux of the trace element in the melt transferred from lithology A to lithology B (the last term). Equation 28c states that the the total melt flux produced by decompression melting of lithology A is the difference in solid mass flux feeding into the melting column from below and solid mass flux at the given location in the melting column. These are general statements of mass flux balance for a non-radioactive chemical species in lithology A in the upwelling steady-state melting column, irrespective of the melting process and whether the partial melt and residual solid are in local equilibrium in the melting column.

3.3. Trace element concentrations in lithology B

Here the conserved form of mass conservation equation for lithology B (Eq. B3) is used to calculate interstitial melt composition. The steady-state version of Eq. B3 takes on the form:

$$\frac{d\left[\rho_f \phi_f^B V_f^B C_f^B + \rho_s\left(1-\phi_f^B\right) V_s^B C_s^B\right]\psi_B}{dz} = \dot{S} C_f^A \tag{29}$$

Similar to the case of lithology A, we replace the melt and solid mass fluxes in Eq. 29 by the degree of melting experienced by lithology B using solutions from the steady-state version of Eqs B1, B2, B6 and B7. The results are as follows:

$$\rho_f \phi_f^B V_f^B = \rho_s V_s^0 F_B + \rho_s V_s^0 \mathbb{R} F_A \frac{\psi_A}{\psi_B} \tag{30a}$$

$$\rho_s\left(1-\phi_f^B\right) V_s^B = \rho_s V_s^0 (1-F_B) \tag{30b}$$

$$F_B = \frac{\Gamma_B z}{\rho_s V_s^0}, \quad k_B = \frac{k_B^0 - k_B^p F_B}{1-F_B} \tag{30c, 30d}$$

The degree of melting experienced by lithology B is related to the degree of melting experienced by lithology A through their melting rates, *i.e.*

$$F_B = \frac{\Gamma_B}{\Gamma_A} F_A \tag{30e}$$

Substituting Eqs 30a–30b into Eq. 29 and replacing z by F_A via Eqs 30c and 30e, we have:

$$\frac{d\left[\left(\psi_B F_B + \psi_A \mathbb{R} F_A\right) C_f^B + \psi_B (1 - F_B) C_s^B\right]}{dF_A} = \mathbb{R} \psi_A C_f^A \tag{31}$$

Equation 31 can be integrated along the melting column, starting from the solidus of lithology B,

$$\left(\psi_B F_B + \psi_A \mathbb{R} F_A\right) C_f^B + \psi_B (1 - F_B) C_s^B = \psi_B C_B^0 + \mathbb{R} \psi_A \int_0^{F_A} C_f^A \, dF_A \tag{32a}$$

Recalling the definition of average melt composition for lithology A (Eq. 24), we have:

$$\left(\psi_B F_B + \psi_A \mathbb{R} F_A\right) C_f^B + \psi_B (1 - F_B) C_s^B = \psi_B C_B^0 + \mathbb{R} \psi_A F_A \bar{C}_f^A \tag{32b}$$

Equation 32b states that the sum of mass flux of the element of interest in the interstitial melt and residual solid in lithology B (left hand side) is balanced by the mass flux of the element in the mantle source of lithology B feeding into the melting column from below and the melt flux flowing from lithology A into lithology B in the melting column (right hand side). When the melt and residual solid are in local chemical equilibrium, we obtain the following expressions for concentrations of the trace element in the melt and residual solid in lithology B:

$$C_f^B = \frac{\psi_B C_B^0 + \psi_A \mathbb{R} F_A \bar{C}_f^A}{\psi_B\left[k_B^0 + \left(1 - k_B^p\right) F_B\right] + \psi_A \mathbb{R} F_A} \tag{33a}$$

$$C_s^B = k_B C_f^B \tag{33b}$$

When $\mathbb{R} = 0$, no melt is transferred from lithology A to lithology B. Equation 33a is reduced to the non-modal batch melting model for lithology B. Hence Eq. 33a is a more general model for batch melting in which an external melt source contributes to the interstitial melt composition. For this reason, we refer to Eq. 33a as the fluxed batch melting model. Interestingly, we can obtain a similar expression for the interstitial melt in lithology A. Rearranging Eq. 28a, we have:

$$C_f^A = \frac{C_A^0 - \mathbb{R} F_A \bar{C}_f^A}{k_A^0 + \left(1 - k_A^p\right) F_A - \mathbb{R} F_A} \tag{33c}$$

Equation 33c can be interpreted as a 'defluxed' batch melting model, as part of the melt proudced has been removed from lithology A.

4. Two continuous melting models

The 'continuous melting model', also referred to in the literature as the 'dynamic melting model', has been used widely in geochemical studies of mantle-derived rocks. In the continuous melting model, a constant and uniform fraction of melt is retained in the residuum after an initial stage of batch melting (*e.g.* Langmuir *et al*., 1977; McKenzie, 1985; Albarède, 1995; Zou, 1998; Shaw, 2000). Any additional melt produced by melting is instantaneously removed from residual solid through an unspecified mechanism. Flows of the melt and solid are not considered explicitly in this class of melting models. Here we use steady-state mass conservation equations to derive the continuous melting model. Following the spirit of continuous melting, we assume that melting in the lower part of the melting column is characterized by batch melting (*i.e.* $\mathbb{R} = 0$). In the upper part of the melting column, a fraction of melt produced in lithology A at a given location is sucked into lithology B at a constant rate (Fig. 1b). We consider two choices of the relative melt suction rate. We show that the continuous or dynamic melting model discussed in the literature is equivalent to the steady-state melting model for a specific choice of melt suction rate (section 4.1) and that porosity in the melting column is not constant and uniform (section 5). We seek an alternative model for continuous melting in which porosity in lithology A in the upper part of the melting column is constant and uniform (section 4.2). Sections E2 and E3 in Appendix E summarize the main results.

4.1. Case of constant melt-to-solid mass flux ratio: The continuous melting model

For readability and convenience of derivation, the steady-state conservation equations for lithology A are relisted below:

$$\left[\rho_f \phi_f^A V_f^A + \rho_s \left(1 - \phi_f^A\right) V_s^A k_A\right] \frac{dC_f^A}{dz} = \left(k_A^p - 1\right) C_f^A \Gamma_A \tag{34a}$$

$$\frac{d\rho_f \phi_f^A V_f^A \psi_A}{dz} = \psi_A \Gamma_A - \dot{S} \tag{34b}$$

$$\frac{d\rho_s\left(1-\phi_f^A\right)V_s^A\psi_A}{dz} = -\psi_A\Gamma_A \tag{34c}$$

$$V_s^A\frac{dF_A}{dz} = \frac{(1-F_A)\Gamma_A}{\rho_s\left(1-\phi_f^A\right)} \tag{34d}$$

$$V_s^A\frac{dk_A}{dz} = \frac{\left(k_A-k_A^p\right)\Gamma_A}{\rho_s\left(1-\phi_f^A\right)} \tag{34e}$$

The boundary conditions at the solidus are:

$$C_f^A(0) = \frac{C_A^0}{k_A^0},\ F_A = \phi_f^A = 0,\ V_s^A = V_s^0,\ k_A = k_A^0 \tag{34f}$$

For constant and uniform melting rate, solutions for the solid mass flux, degree of melting and bulk partition coefficient are the same as before, *i.e.*

$$\rho_s\left(1-\phi_f^A\right)V_s^A = \rho_s V_s^0(1-F_A), F_A = \frac{\Gamma_A z}{\rho_s V_s^0},\ \ k_A = \frac{k_A^0-k_A^p F_A}{1-F_A} \tag{35}$$

Equation 34a can be integrated given the melt flux in lithology A. Following the spirit of continuous melting, we assume that the melt suction rate in the lower part of the melting column ($F_A < F_A^d$) is zero. Instead of solving the melt flux from Eq. 34b for a given melt suction rate, here we consider a special case in which the ratio between the melt mass flux and the solid mass flux in lithology A (designated as ω) is constant and uniform in the upper part of the melting column (Liang, 2008). To ensure mass conservation, we require that the melt flux at the boundary that divides the upper and lower melting column is continuous. Hence the melt flux in lithology A in the melting column takes on the form:

$$\rho_f\phi_f^A V_f^A = \begin{cases} \rho_s V_s^0 F_A & \text{for } F_A < F_A^d \\ \omega\left[\rho_s V_s^0(1-F_A)\right] & \text{for } F_A \geq F_A^d \end{cases} \tag{36a}$$

$$F_A^d = \frac{\omega}{1+\omega} \tag{36b}$$

where F_A^d is the degree of melting at which the melt fluxes from the two expressions in Eq. 36a are equal. We will discuss the physical meaning of ω at the end of this derivation. Substituting Eq. 36a in Eq. 34a, we obtain a set of ordinary differential equations for the melt composition. In terms of degree of melting experienced by lithology A, we have:

$$[F_A + (1 - F_A)k_A]\frac{dC_f^A}{dF_A} = \left(k_A^p - 1\right)C_f^A, \quad \text{for } F_A < F_A^d \tag{37a}$$

$$(1 - F_A)(\omega + k_A)\frac{dC_f^A}{dF_A} = \left(k_A^p - 1\right)C_f^A, \quad \text{for } F_A \geq F_A^d \tag{37b}$$

Equations 37a–37b can be integrated sequentially, starting from the solidus of lithology A. We have:

$$C_f^A = \frac{C_A^0}{k_A^0 + \left(1 - k_A^p\right)F_A}, \quad \text{for } F_A < F_A^d \tag{38a}$$

$$C_f^A = \left[\frac{C_A^0}{k_A^0 + \left(1 - k_A^p\right)F_A^d}\right]\left[\frac{k_A^0 + \omega - \left(k_A^p + \omega\right)F_A}{k_A^0 + \omega - \left(k_A^p + \omega\right)F_A^d}\right]^{\frac{1 - k_A^p}{k_A^p + \omega}} \quad \text{for } F_A \geq F_A^d \tag{38b}$$

In mathematical forms, Eqs 38a–38b are identical to the continuous or dynamic melting model discussed in the literature (*e.g.* McKenzie, 1985; Albarède, 1995; Zou, 1998; Shaw, 2000). In the previous treatment of continuous melting, ω in Eq. 38b is replaced by a melting parameter α which is the ratio between mass density of the melt and mass density of the solid in a unit volume of the partially molten system (*e.g.* Shaw, 2000),

$$\alpha = \frac{\rho_f \phi_f^A}{\rho_s\left(1 - \phi_f^A\right)} \quad \text{and} \quad F_A^d = \frac{\alpha}{1 + \alpha} = \frac{\rho_f \phi_f^A}{\rho_f \phi_f^A + \rho_s\left(1 - \phi_f^A\right)} \tag{39}$$

In the model presented above, ω is the ratio between the mass flux of the melt and the mass flux of the solid in lithology A, *i.e.*

$$\omega = \frac{\rho_f \phi_f^A V_f^A}{\rho_s\left(1 - \phi_f^A\right)V_s^A} \quad \text{and} \quad F_A^d = \frac{\rho_f \phi_f^A V_f^A}{\rho_f \phi_f^A V_f^A + \rho_s\left(1 - \phi_f^A\right)V_s^A} \tag{40}$$

The melt velocity is generally larger than the solid velocity in the melting column (*i.e.* $V_f^A > V_s^A$). Hence one would overestimate the melt fraction in residual solid in an upwelling melting column using the continuous melting model with melting parameters defined by Eq. 39.

In the steady-state melting model described in section 3.1, the dimensionless melt suction rate takes on a constant value in the entire melting column ($0 \leq \mathbb{R} \leq 1$). The melt flux increases linearly upwards, independent of the solid mass flux. In the continuous or dynamic melting model, the dimensionless melt suction rate takes on two constant values in the melting column:

$$\mathbb{R} = \frac{\dot{S}}{\psi_A \Gamma_A} = \begin{cases} 0 & \text{for } F_A < F_A^d \\ 1 + \omega & \text{for } F_A \geq F_A^d \end{cases} \tag{41}$$

Equation 41 is obtained from the mass conservation equation for interstitial melt (Eq. 34b) using the prescribed melt flux of Eq. 36a. Hence in the context of decompression melting, the continuous melting model is characterized by batch melting in the lower part of the melting column ($F_A < F_A^d$) and steady-state melting with a constant melt suction rate of $1 + \omega$ in the upper part of the melting column ($F_A \geq F_A^d$) where the mass flux ratio between the melt and solid takes on a constant value of ω. The greater than unit dimensionless melt suction rate ($1 + \omega$) in the upper part of the melting column arises from the influx of batch melt at $F_A = F_A^d$.

Finally, given the interstitial melt composition (Eq. 38a–38b) and melt suction rate (Eq. 41) for lithology A, we can use the conserved form of mass conservation equation to calculate concentrations of the trace element in the melt and residual solid in lithology B. Integrating Eqs 25 and 29, we have:

$$C_f^B = \frac{C_B^0}{k_B^0 + \left(1 - k_B^p\right) F_B}, \quad \text{for } F_A < F_A^d \tag{42a}$$

$$C_f^B = \frac{\psi_B C_B^0 + \psi_A (1 + \omega)\left(F_A - F_A^d\right) \bar{C}_f^A}{\psi_B\left[k_B^0 + \left(1 - k_B^p\right) F_B\right] + \psi_A (1 + \omega)\left(F_A - F_A^d\right)}, \quad \text{for } F_A \geq F_A^d \tag{42b}$$

where the average concentration of melts transferred from lithology A to lithology B is defined as:

$$\bar{C}_f^A = \frac{1}{F_A - F_A^d} \int_{F_A^d}^{F_A} C_f^A \, dF_A = \frac{C_A^0 - \left[k_A^0 + \omega - \left(k_A^p + \omega\right) F_A\right] C_f^A}{(1 + \omega)\left(F_A - F_A^d\right)}, \quad \text{for } F_A \geq F_A^d \tag{42c}$$

Note that in Eq. 42c batch melts are excluded from the integration because they are not extracted to lithology B in the lower part of the melting column.

4.2. Case of constant melt mass flux: The constant porosity model

The assumption of constant and uniform melt-to-solid mass flux ratio in the upper part of the melting column in lithology A is somewhat arbitrary. It is used for the convenience of model derivation and comparison with the continuous melting model. A different set of melting models can be obtained by assuming, for example, a constant melt flux in the upper part of the melting column in lithology A, *i.e.*

$$\rho_f \phi_f^A V_f^A = \begin{cases} \rho_s V_s^0 F_A & \text{for } F_A < F_A^d \\ \rho_s V_s^0 F_A^d & \text{for } F_A \geq F_A^d \end{cases} \tag{43}$$

This condition can be realized when the dimensionless melt suction rate takes on the following values in melting column:

$$\mathbb{R} = \frac{\dot{S}}{\psi_A \Gamma_A} = \begin{cases} 0 & \text{for } F_A < F_A^d \\ 1 & \text{for } F_A \geq F_A^d \end{cases} \tag{44}$$

The concentration of the trace element in the melt in lithology A takes on the expressions

$$C_f^A = \frac{C_A^0}{k_A^0 + \left(1 - k_A^p\right) F_A}, \quad \text{for } F_A < F_A^d \tag{45a}$$

$$C_f^A = \left[\frac{C_A^0}{k_A^0 + \left(1 - k_A^p\right) F_A^d}\right] \left[\frac{k_A^0 + F_A^d - k_A^p F_A}{k_A^0 + \left(1 - k_A^p\right) F_A^d}\right]^{\frac{1 - k_A^p}{k_A^p}}, \quad \text{for } F_A \geq F_A^d \tag{45b}$$

The concentration of the trace element in the melt in lithology B is given by:

$$C_f^B = \frac{C_B^0}{k_B^0 + \left(1 - k_B^p\right) F_B}, \quad \text{for } F_A < F_A^d \tag{45c}$$

$$C_f^B = \frac{\psi_B C_B^0 + \psi_A \left(F_A - F_A^d\right) \bar{C}_f^A}{\psi_B \left[k_B^0 + \left(1 - k_B^p\right) F_B\right] + \psi_A \left(F_A - F_A^d\right)}, \quad \text{for } F_A \geq F_A^d \tag{45d}$$

where the average concentration of melts transferred from lithologies A to B is defined as:

$$\bar{C}_f^A = \frac{1}{F_A - F_A^d} \int_{F_A^d}^{F_A} C_f^A \, dF_A = \frac{C_A^0 - \left(k_A^0 + F_A^d - k_A^p F_A\right) C_f^A}{F_A - F_A^d}, \quad \text{for } F_A \geq F_A^d \tag{45e}$$

Equation 45b is slightly different from Eq. 38b for the continuous melting model. We will compare these two models in sections 5 and 6.

5. A general two-lithology melting model

The melt suction rate in the upper part of the melting column takes on the special value of 1 or $1 + \omega$ in the two cases presented in section 4. In a more general case, the constant melt suction rate in the upper part of the melting column can take on a range of values, from <1 to >1 and the degree of melting or depth that divides the two melting regimes (F_A^d) does not have to be related to the melting parameter ω. In this section, this more general case of steady-state melting is considered. We start with mass conservation for the interstitial melt in lithology A which takes on the form:

$$\frac{d\rho_f \phi_f^A V_f^A \psi_A}{dz} = \psi_A \Gamma_A, \quad \text{for } F_A < F_A^d \tag{46a}$$

$$\frac{d\rho_f \phi_f^A V_f^A \psi_A}{dz} = \psi_A \Gamma_A - \dot{S}, \quad \text{for } F_A \geq F_A^d \tag{46b}$$

where the melt suction rate in Eq. 46b is a constant. Integrating Eqs 46a–46b from the solidus, we have the melt flux in lithology A:

$$\rho_f \phi_f^A V_f^A = \begin{cases} \rho_s V_s^0 F_A & \text{for } F_A < F_A^d \\ \rho_s V_s^0 (1 - \mathbb{R}) F_A + \rho_s V_s^0 F_A^d \mathbb{R} & \text{for } F_A \geq F_A^d \end{cases} \tag{47}$$

The second term on the right-hand-side of Eq. 47 is the influx of excess melt from the lower part of the melting column ($F_A < F_A^d$) where the melt suction rate is zero. The dimensionless melt suction rate (Eq. 17c) is a constant that can take on values of $0 \leq \mathbb{R} \leq \mathbb{R}_{\max}$ in the upper part of the melting column. The upper bound for the dimensionless melt suction rate ($\mathbb{R}_{\max}$) is constrained by the condition when the melt flux in lithology A becomes zero. From Eq. 47, we have the upper bound:

$$\mathbb{R}_{\max} = \frac{F_A^{\max}}{F_A^{\max} - F_A^d} \tag{48}$$

where $F_A^{\max}$ is the maxium extent of melting experienced by lithology A at top of the melting column. For $F_A^{\max} = 20\%$ and $F_A^d = 5\%$, we have $\mathbb{R}_{\max} = 1.33$.

Expressions for the mass flux of solid and degree of melting are the same as the two cases discussed in section 4 (Eq. 35). Substituting the melt and solid mass fluxes into the mass conservation equation for trace elements (Eq. 34a) and upon integration, we obtain the following expressions for the concentration of a trace element in the interstitial melt in lithology A:

$$C_f^A = \frac{C_A^0}{k_A^0 + \left(1 - k_A^p\right)F_A}, \quad \text{for } F_A < F_A^d \tag{49a}$$

$$C_f^A = \left[\frac{C_A^0}{k_A^0 + \left(1 - k_A^p\right)F_A^d}\right]\left[\frac{k_A^0 + F_A^d\mathbb{R} + \left(1 - k_A^p - \mathbb{R}\right)F_A}{k_A^0 + \left(1 - k_A^p\right)F_A^d}\right]^{\frac{k_A^p - 1}{1 - k_A^p - \mathbb{R}}}, \quad \text{for } F_A \geq F_A^d. \tag{49b}$$

Solutions for the concentration of the trace element in the interstitial melt in lithology B are

$$C_f^B = \frac{C_B^0}{k_B^0 + \left(1 - k_B^p\right)F_B}, \quad \text{for } F_A < F_A^d \tag{49c}$$

$$C_f^B = \frac{\psi_B C_B^0 + \psi_A \mathbb{R}\left(F_A - F_A^d\right)\bar{C}_f^A}{\psi_B\left[k_B^0 + \left(1 - k_B^p\right)F_B\right] + \psi_A \mathbb{R}\left(F_A - F_A^d\right)}, \quad \text{for } F_A \geq F_A^d \tag{49d}$$

where the average concentration of melts transferred from lithologies A to B is defined as:

$$\bar{C}_f^A = \frac{1}{F_A - F_A^d}\int_{F_A^d}^{F_A} C_f^A dF_A = \frac{C_A^0 - \left[k_A^0 + \mathbb{R}F_A^d + \left(1 - k_A^p - \mathbb{R}\right)F_A\right]C_f^A}{\mathbb{R}\left(F_A - F_A^d\right)}, \quad \text{for } F_A \geq F_A^d \tag{49e}$$

Finally, the melt and solid mass fluxes in lithology B are

$$\rho_f \phi_f^B V_f^B \psi_B = \begin{cases} \rho_s V_s^0 F_B \psi_B & \text{for } F_A < F_A^d \\ \rho_s V_s^0\left[F_B\psi_B + \mathbb{R}\left(F_A - F_A^d\right)\psi_A\right] & \text{for } F_A \geq F_A^d \end{cases} \tag{49f}$$

$$\rho_s\left(1 - \phi_f^B\right)V_s^B = \rho_s V_s^0\left(1 - F_B\right) \tag{49g}$$

Equations 49a–49b unify the simple models for trace element fractionation during decompression melting in an upwelling melting column in which the melt suction rate takes on one or two constant values. In addition to partition coefficients, there are three physical parameters in this melting model: degree of melting experienced by the residuum (F_A), the depth or degree of melting above which interstitial melt flows from lithology A to lithology B (F_A^d) and the dimensionless melt suction rate ($\mathbb{R}$). Different choices of these melting parameters lead to different melting models presented in the preceding sections. Specifically, Eqs 49a–49b are reduced to:

(a) the batch melting model when $\mathbb{R} = 0$;
(b) the perfect fractional melting model when $\mathbb{R} = 1$ and $F_A^d = 0$;
(c) the two-porosity melting model with constant and uniform melt suction rate (Eq. 21a) when $0 < \mathbb{R} < 1$ and $F_A^d = 0$;
(d) the continuous melting model with constant melt flux or porosity when $\mathbb{R} = 1$ in the upper part of the melting column; and
(e) the continuous or dynamic melting model discussed in the literature when $\mathbb{R} = 1 + \omega$ and $F_A^d = \omega/(1 + \omega)$.

Figure 2 summarizes these results. When the volume fraction of lithology B is reduced to zero ($\psi_B = 0$), the melt composition of lithology B (Eq. 49d) equals to the average melt composition of lithology A, *i.e.* $C_f^B = \bar{C}_f^A$. The average melt composition from lithology A has been used widely in modelling trace elements and isotope ratios in pooled melt derived from partial melting of a single lithology source.

Another case of special interest is when lithology B is dunite in the upper part of the melting column. The melting rate of dunite is neglegible. Melt composition in dunite channels varies along the melting column according to the fraction of melt transferred from lithology A to lithology B. Let F_B^{dunite} be the extent of melting at which pyroxene-free dunite is formed from lithology B. Melt composition in the dunite channel is given by the expression:

$$C_f^B = \frac{\psi_B C_B^0 + \psi_A \mathbb{R}\left(F_A - F_A^d\right)\bar{C}_f^A}{\psi_B\left[k_B^0 + \left(1 - k_B^p\right)F_B^{dunite}\right] + \psi_A \mathbb{R}\left(F_A - F_A^d\right)} \tag{50}$$

where the first terms in the numerator and the denominitor account for dunite formation. Hence, melt composition in the dunite channel is a mixture of melts transferred from lithology A to lithology B and the melt produced by converting lithology B to dunite (*via* partial melting and reactive dissolution). For transport of incompatible trace elements in dunite channels, we can further simplify Eq. 50 by setting partition coefficients in lithology B to zero, *i.e.*

$$C_f^B = \frac{\psi_B C_B^0 + \psi_A \mathbb{R}\left(F_A - F_A^d\right)\bar{C}_f^A}{\psi_B F_B^{dunite} + \psi_A \mathbb{R}\left(F_A - F_A^d\right)} \tag{51}$$

Equation 51 indicates that formation of dunite channels in the melting column results in a dilution of incompatible trace element concentrations in the channel melt, *i.e.* $C_f^B < \bar{C}_f^A$.

This effect, which has not been considered in most two-porosity melting models in the literature, may provide a simple mechanism for producing highly depleted melts, such as those observed in some olivine-hosted melt inclusions (*e.g.* Sobelev and Shimizu, 1994; Shimizu, 1998).

In summary, Eqs 49a–49g are a set of more general solutions for trace element fractionation during decompression melting in an upwelling two-lithology melting column. This new model features batch melting in the lower part of the melting column for both lithology A and lithology B, steady-state melting with a constant melt suction rate in the upper part of the melting column for lithology A and fluxed batch melting in the upper part of the melting column for lithology B. It recovers the batch melting, fractional melting, continuous melting and two-porosity melting models under specific limits. To minimize confusion with the previous melting models, we call this more general steady-state melting model (Eqs 49a–49g, 8–9) the two-lithology melting model. In the next section, we show that this two-lithology melting model also has two porosities.

6. Porosity in the two-lithology melting column

Porosity or melt fraction in an upwelling melting column depends primarily on the melt flux. Hence, porosities in the two lithologies vary along the melting column and are different for different choices of the melt suction rate. To further differentiate the various melting models considered in this study, we use Darcy's law to calculate porosities in the upwelling melting column for a given set of melt suction rates. Appendix D provides a derivation of porosities for the two-lithology melting model presented in section 5. Approximate expressions for the porosity in lithology A are:

$$\phi_f^A \approx \phi_{ref}^A \left(\frac{F_A}{F_A^{\max}} \right)^{\frac{1}{3}}, \quad \text{for } F_A < F_A^d \tag{52a}$$

$$\phi_f^A \approx \phi_{ref}^A \left[\frac{(1-\mathbb{R})F_A + \mathbb{R}F_A^d}{F_A^{\max}} \right]^{\frac{1}{3}}, \quad \text{for } F_A \geq F_A^d \tag{52b}$$

Similarly, for lithology B, we have:

$$\phi_f^B \approx \phi_{ref}^B \left(\frac{F_B}{F_B^{\max}} \right)^{\frac{1}{3}}, \quad \text{for } F_A < F_A^d \tag{53a}$$

$$\phi_f^B \approx \phi_{ref}^B \left[\frac{\psi_B F_B + \psi_A \mathbb{R}\left(F_A - F_A^d\right)}{\psi_B F_B^{\max}} \right]^{\frac{1}{3}}, \quad \text{for } F_A \geq F_A^d \tag{53b}$$

Here ϕ_{ref}^{A} and ϕ_{ref}^{B} are reference porosities for lithology A and lithology B defined in Eqs D5a–D5b in Appendix D. The two reference porosities are related to each other via the relationship:

$$\phi_{ref}^{B} = \left(\frac{F_{B}^{\max} d_{A}^{2}}{F_{A}^{\max} d_{B}^{2}}\right)^{\frac{1}{3}} \phi_{ref}^{A} = \left(\frac{\Gamma_{B} d_{A}^{2}}{\Gamma_{A} d_{B}^{2}}\right)^{\frac{1}{3}} \phi_{ref}^{A} \qquad (54)$$

where d_A and d_B are average grain sizes of lithology A and lithology B, respectively. If $F_{B}^{\max} = 2F_{A}^{\max}$, $d_A = d_B$ and $\phi_{ref}^{A} = 2\%$, we have $\phi_{ref}^{B} = 2.5\%$. Hence porosities in the two lithologies are generally different for different choices of melting rate and grain size.

Given the reference porosities, we can calculate variations of porosity in the two lithologies in the melting column. Figure 3a displays porosity variations in lithology A (solid lines) and lithology B (dashed lines) for five choices of the melt suction rate. In response to melting, porosities increase upwards for a given melt suction rate in the two lithologies. With increasing melt suction rate, porosity in lithology A decreases, whereas porosity in lithology B increases at a given depth in the melting column. For perfect fractional

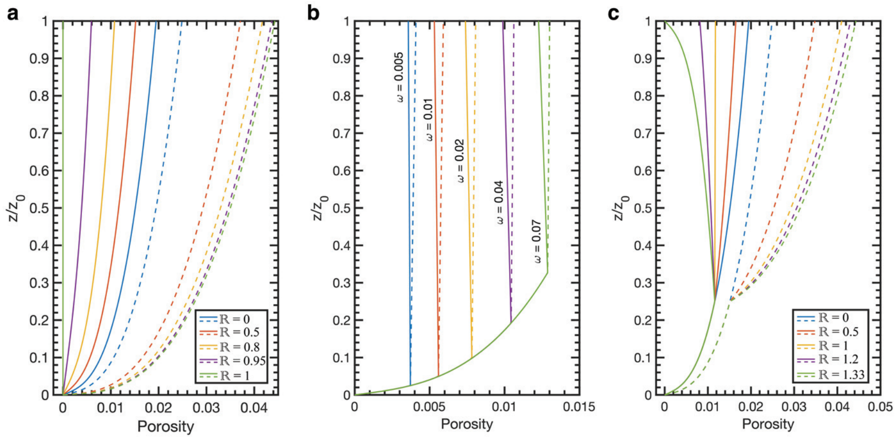

Fig. 3. (***a***) Spatial variations in porosity in lithology A (solid curves) and lithology B (dashed curves) in the melting column for decompression melting with a constant and uniform melt suction rate. (***b***) Variations in porosity in lithology A during continuous melting with constant melt-to-solid mass flux ratio (solid lines) or constant melt flux (dashed lines) in the upper part of the melting column. (***c***) Variations in porosity in lithology A (solid curves) and lithology B (dashed curves) in the melting column according to the two-lithology melting model in which batch melting takes place in the lower quarter of the melting column in the two lithologies. Five choices of melting parameters are provided in respective panels. Porosities in the three panels are solved numerically from Eqs D6a and D6b using the MATLAB function fzero. Porosity obtained from the approximate solutions (Eqs 52–55, not shown here) are slightly smaller than the 'exact' values (by $<5\%$, relative). Note, there is a very small upwards increase in porosity for the case of constant melt flux (dashed lines in Fig. 2b). This is due to the upwards reduction in the solid volume flux, which is second order (the third term in the square bracket of Eq. D4a) and is ignored in the approximate solution (Eq. 52b).

melting, porosity in lithology A is zero in the melting column while porosity in lithology B reaches maximum values along the melting column (cf. green solid and dashed lines in Fig. 3a).

Figure 3b compares porosity distributions in lithology A for the case of constant melt-to-solid mass flux ratio (solid lines) and the case of constant melt flux (dashed lines) in the upper part of the melting column for five choices of the melting parameter ω ($\mathbb{R} = 1 + \omega$) or F_A^d. In terms of trace element fractionation, the case of constant melt-to-solid mass flux ratio is equivalent to the continuous or dynamic melting model used in the literature. As more melt is transferred from lithology A to lithology B than that produced in lithology A in this part of the melting column ($\mathbb{R} > 1$), the porosity in lithology A decreases upwards in the melting column in the continuous melting model (solid lines in Fig. 3b). This is in contrast with the assumption of constant porosity used in the derivation of the continuous melting model in the literature (*e.g.* McKenzie, 1985; Albarède, 1995; Zou, 1998; Shaw, 2000).

The porosity in lithology A is effectively constant and uniform in the upper region of the melting column when the amount of melt produced in lithology A by melting is balanced by the amount of melt transferred from lithology A to lithology B. This is the case when $\mathbb{R} = 1$. From Eq. 52b, we have an approximate expression for the porosity in the upper part of lithology A:

$$\phi_f^A \approx \phi_{ref}^A \left(\frac{F_A^d}{F_A^{\max}} \right)^{\frac{1}{3}}, \quad \text{for } F_A \geq F_A^d \tag{55}$$

If $F_A^d = 5\%$, $F_A^{\max} = 20\%$ and $\phi_{ref}^A = 2\%$, we have $\phi_f^A = 1.26\%$. The case of constant melt flux is shown as vertical dashed lines in Fig. 3b. In general, porosities derived from the constant melt-to-solid mass flux ratio model are slightly smaller than porosities derived from the constant melt flux model for the same amount of batch melting in the lower part of the melting column (cf. solid *vs.* dashed lines of the same colour in Fig. 3b).

Figure 3c displays porosity distributions in lithology A (solid lines) and lithology B (dashed lines) for the two-lithology melting model. In this example, batch melting takes place in the lower quarter of the melting column ($\mathbb{R} = 0$) and the melt suction rate in the upper part of the melting column takes on a wide range of values. When $0 \leq \mathbb{R} < 1$ in the upper three quarters of the melting column, only part of the melt generated in lithology A is transferred to lithology B. The remaining melt percolates upwards in lithology A, resulting in an upwards increase in porosity in lithology A. When $\mathbb{R} = 1$, the porosity and melt flux in lithology A remain constant and uniform in the upper three quarters of the melting column. When $1 < \mathbb{R} \leq \mathbb{R}_{\max}$, more melt is transferred from lithology A to lithology B than that produced in lithology A in the upper three quarters of the melting column. Consequently, the porosity in lithology A decreases upwards. Regardless of the melt suction rate, the porosity in lithology B increases upwards in the melting column. The larger the melt suction rate, the larger the porosity is in lithology B.

In summary, porosities in lithologies A and B in the two-lithology melting model take on a range of values, depending on the melting parameters. They recover the special cases displayed in Figs 3a-3b under stated limits. Furthermore, porosities in lithology A and lithology B are continuous along the melting column. This is in contrast with previous two-porosity melting models in which porosity of the channel is discontinuous in the melting column (*e.g.* Jull *et al.*, 2002). The discontinuous channel porosity results from the assumption of instantaneous channel formation at a prescribed depth in the melting column. In our models, high-porosity channels are formed gradually in lithology B. The discontinuity in porosity gradient in the models shown in Figs 3b and 3c is due to the assumption of constant melt suction rate in the upper part of the melting column. This discontinuity can be eliminated by allowing the melt suction rate to vary continuously in the melting column, starting from zero in the lower part of the melting column. Finally, we note that given the melting parameters, Eqs 52–53 can be used to infer porosities in the melting column. Liang and Peng (2010) provided an example in which they used the extent of melting and melt suction rate derived from REE patterns in clinopyroxene in residual abyssal peridotites to calculate the porosity and permeability in the meting region beneath mid-ocean ridge spreading centers.

7. Variations in melt composition

In this section we use the two-lithology melting model (Eqs. 49a-49e) to illustrate how REE in interstitial melts in lithology A and lithology B, average melt in lithology A and mixed-column melt bewteen the two lithologies in the melting column vary as a function of the degree of melting experienced by lithology A (F_A) or lithology B (F_B). For a given melting rate, the degree of melting scales with the column height (Eqs. 16 or 30c). Melt compositions at different locations in a tall melting column (*e.g.* column 10 in the inset to Fig. 4c) can also be taken as melt compositions at top of shorter melting columns (columns 1 to 9). We consider two cases: lithology B is dunite in the upper part of the melting column (section 7.1); and (2) lithology B is a pyroxenite (section 7.2 and section 7.3).

7.1. Dilution effect due to dunite channel formation in the melting column

To highlight the dilution effect, we consider decompression melting of a homogeneous mantle (lherzolite = 15% Cpx + 28% Opx + 57% olivine) in which lithology A and lithology B have the same composition and lithology in the mantle source. A fraction of the residual mantle (identified as lithology B) is transformed into pyroxene-free dunite through a combination of fluxed melting and reactive dissolution. For the purpose of demonstration, we assume that the combined melting and dissolution rate of lithology B is four times the melting rate of lithology A and that the pyroxenite-free dunite forms in the upper part of lithology B when $F_B = F_{dunite} = 50\%$. Figure 4a shows that REE concentrations in the interstitial melt in lithology A are depleted progressively by a combination of 4% batch melting followed by 16% continuous melting

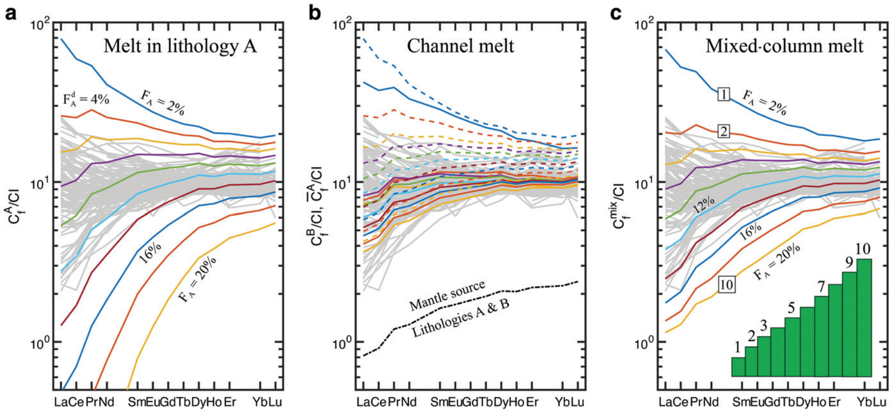

Fig. 4. Chondrite normalized REE patterns in interstitial melts in lithology A (***a***) and lithology B (***b***, solid lines), average melts transferred from lithology A to lithology B (dashed lines in ***b***), and mixed-column melts at top of melting columns (***c***) produced by decompression melting of a homogeneous mantle with channelized melt migration in lithology B. Curves of the same colour correspond to a set of melt compositions produced by the same extent of melting (at 2% increment in F_A). The mixed-column melts 1, 2, …, 10 correspond to the numbered melting columns in the inset in panel (***c***). The mantle sources for lithology A and lithology B have the same lithology (lherzolite = 15% Cpx, 28% Opx and 57% olivine) and composition (DMM of Workman and Hart, 2005, dash-dotted line in panel ***b***). For simplicity, we ignore spinel in the REE modelling. REE concentrations are calculated using Eqs 49a–49e, Eq. 50, and Eq. 8 with the following melting parameters: $\mathbb{R} = 1$ and $F_A^d = 4\%$. The maximum extent of melting for lithology A is 20% and the maximum extent of melting for lithology B is 50% at which pyroxene-free dunite forms. Mineral-melt REE partition coefficients are from Sun and Liang (2012, 2013) and Yao *et al.* (2012). For demonstration, we assume non-modal melting for the lherzolite and modal melting for lithology B. Melting reaction for the lherzolite is 0.79 Cpx + 0.41 Opx = 0.2 olivine + melt (modified from Walter, 2014). REE patterns in the dunite are not sensitive to the details of how pyroxenes are exhausted in the residual solid. Hence it is sufficient to use modal melting for lithology B in this example. The background gray lines are REE in olivine-hosted melt inclusions from the FAMOUS segment of the Mid-Atlantic Ridge (Shimizu, 1998; Laubier *et al.*, 2012).

($\mathbb{R} = 1$) of the starting lherzolite (solid curves with 2% increment in F_A). The LREE depleted patterns are typical of fractional or near fractional melting of lherzolite. During near fractional melting of lithology A (lherzolite), a large fraction of melt produced in lithology A is transferred to lithology B (high-porosity channels), resulting in strong depletion in incompatible trace elements in the residuum.

The interstitial melt in dunite channels is a mixture of melts transferred from lithology A to lithology B and melts produced by dissolution of pyroxene and precipitation of olivine in lithology B. Figure 4b shows that the interstitial melt in lithology B (solid lines, Eqs 49d and 50) is more depleted than the average melt from lithology A (dashed lines, Eq. 49e) at a given location in the melting column (lines of the same colour). The extent of dilution depends on the fraction of dunite in the melting column (ψ_B) and the 'degree of melting' at which dunite channel initiates (F_{dunite}): the larger the ψ_B and F_{dunite}, the stronger the dilution effect (cf. Eq. 51). However, the extent of dilution is not sensitive to the details of how pyroxenes are exhausted in the residual solid, *i.e.* whether it is by melting or dissolution. The average melt from lithology A has been used widely as the channel melt in the literature. Here we show that incompatible trace elements in the channel melt are diluted by the dunite formation reaction: pyroxene + melt$_1$ = olivine + melt$_2$, where melt$_1$ is the melt transferred from lithology A to lithology B; and melt$_2$ is the interstitial melt in the dunite channel. Unlike melt$_2$, melt$_1$ cannot be sampled in the melting column or at its top.

Finally, for the depleted starting mantle composition, LREE abundances in the mixed-column melt and interstitial melts are depleted progressively by melting (Fig. 4a–4c). Figure 4c shows that the LREE-depleted patterns in olivine-hosted melt inclusions from the FAMOUS segment of the Mid-Atlantic Ridge (Shimizu, 1998; Laubier *et al.*, 2012) can be explained by the high degree of mixed-column melts ($8\% < F_A < 16\%$) or melts from incomple mixing of mixed-column melts from short and tall melting columns (not shown). These LREE depleted patterns are broadly similar to those observed in D-MORB and N-MORB. However, the flat and LREE-enriched patterns may require an enriched mantle source which we will explore below.

7.2. Melting a two-lithology mantle: Two incompatible trace elements

The presence of a second lithology changes the bulk partition coefficient and the extent of melting for lithology B, resulting in additional fractionation of the trace element of interest. To set up a stage for the more practical examples presented in section 7.3, we first compare two trace elements with constant bulk partition coefficients of (0.01, 0.03) and (0.1, 0.3) in the two lithologies (A, B). For the purpose of illustration, we assume that concentrations of the two incompatible trace elements in lithology B in the mantle source are 10 times those in lithology A and that the melting rate of lithology B is twice that of lithology A.

Figure 5a,c displays concentrations of the two trace elements in the interstitial melt (solid curves) and average melt (dashed lines) in lithology A for five choices of the melt suction rate. Three general observations can be made. First, incompatible trace element cocentrations in interstitial melts become more and more depleted with increasing melt suction rate and extent of melting. The depletion is due to removal of incompatible trace elements in residual solid by melting and in interstitial melt by transport to lithology B. Second, the difference in trace element concentration between the continuous melting model (case of $\mathbb{R} = 1.042$) and the constant melt flux model ($\mathbb{R} = 1$) is small for both the interstitial melt and average melt of lithology A. This is consistent with their small differences in porosity and melt flux as the melt suction rate between the two models is very similar. Finally, concentrations of the two incompatible trace elements in average melts at a given degree of melting are higher than those in interstitial melts produced by batch melting ($\mathbb{R} = 0$). This happens because progressively less melt is left behind in residual solid with increasing melt suction rate (Fig. 3a).

Figure 5b,d compares concentrations of the two incompatible elements in interstitial melt in lithology B (solid curves in the upper part of each panel), average melt from lithology A (solid curves in the lower part of each panel) and mixed-column melt

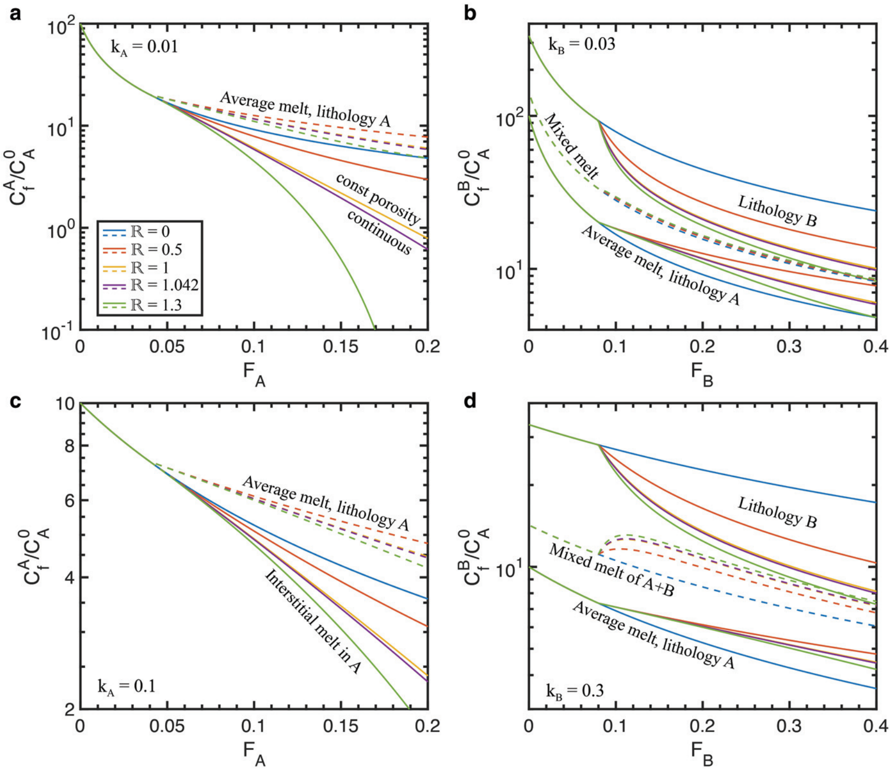

Fig. 5. Variations of two incompatible trace elements in interstitial melts (solid curves) and average melts (dashed curves) in lithology A (***a***, ***c***), interstitial melts in lithology B (upper solid curves) and mixed-column melts (dashed curves) from lithology A and lithology B (***b***, ***d***) as functions of the degree of melting experienced by the two lithologies. Trace element concentrations are calculated for five choices of the melt suction rate (colour-coded curves) using Eqs 49a–49e and Eq. 8 and bulk partition coefficients provided in each panel. For demonstration, we assume modal melting in the two lithologies and that batch melting takes place in the lower fifth of the melting column ($F_A^d = 4\%$). To facilitate comparison, concentrations of the two trace elements in melts are normalized by their respective concentrations in lithology A in the mantle source. Concentrations of the two trace elements in lithology B in the mantle source are ten times those in lithology A.

from the two lithologies (dashed curves). Five general observations can be made. First, incompatible trace element concentrations in interstitial melts in lithology B are less depleted with increasing extent of melting than those in lithology A for a given melt suction rate. This is due to a combination of fluxed batch melting in lithology B and its enriched mantle source composition. Upwards percoloation of lower-degree melts in the deeper part of the melting column to the overlying melting region increases incompatible trace element abundance in the melt, which alleviates the depletion of incompatible trace elements in the overlying melting column. This self-enrichment takes place when lower-degree melts percolate through a higher-degree melting region (*e.g.*

Richter, 1986; Liang, 2008; Liang and Peng, 2010). Second, the dilution effect discussed in section 7.1 and illustrated in Fig. 4b is obscured by the enriched mantle source composition in lithology B (by a factor of 10 relative to lithology A). If we lowered concentrations of the two trace elements in lithology B in mantle source by a factor of 10, the interstitial melts in lithology B would be plotted below the average melts of lithology A in Fig. 5b,d. Third, at a given location or extent of melting, trace element concentrations in the interstitial melt in lithology B decrease with the increase of melt suction rate. This is part of the dilution effect produced by the influx of more depleted melts from lithology A. Fourth, the mixed-column melt from lithology A and lithology B are plotted between the average melt from lithology A and the interstitial melt from lithology B. For highly incompatible trace elements (Fig. 5b), the mixed-column melt compositon is practically independent of the melt suction rate or melting model, as residual solid is depleted extensively by melting (Eqs 9a and 10a). Hence, for highly incompatible trace elements ($k < 0.01$), mixing of melts from lithologies A and B are equivalent to mixing of the two sources, although their proportions are different from those in the mantle source. This can be seen from Eq. 10a in section 2.2. Finally, for moderately incompatible (and compatible) trace elements, mixing of melts from the two lithologies is sensitive to the melt suction rate or melting mechanism. Figure 5d presents one such example.

7.3. Melting a peridotite-pyroxenite mantle: Rare earth elements

Here we consider two examples in which the mantle source of lithology A is the same lherzolite as that used in the example shown in Fig. 4 (15% Cpx + 28% Opx + 57% olivine). The mantle source of lithology B is either a Cpx-rich pyroxenite (60% Cpx + 10% Opx + 30% olivine, Fig. 6a,d) or an Opx-rich pyroxenite (10% Cpx + 60% Opx + 30% olivine, Fig. 6b,e). These secondary pyroxenites can be formed by reaction between a peridotite and melts derived from garnet pyroxenite and eclogite in the deeper part of the mantle column, a process that is not modelled here. The melting rate of the secondary pyroxenite is probably greater than that of the peridotite, although the former is still not well characterized. For the examples presented below, we set the maximum extent of melting to 20% for lithology A and 40% for lithology B. Batch melting takes place in the lower fifth of the melting column. The melt suction rate in the upper four fifths of lithology A is 1, which is the case of constant porosity or constant melt flux melting model (section 4.2). REE abundances in the interstitial melt in lithology A are the same as those shown in Fig. 4a.

Figure 6a–c explores the effect of Opx to Cpx proportion in the pyroxenite on REE patterns in interstitial melts in lithology B and the mixed-column melt at top of the melting column. Here we fix the volume fractions of lherzolite (90%) and pyroxenite (10%) in the mantle source and vary the proportion of Cpx to Opx in lithology B (60:10 *vs.* 10:60, 30% olivine). For a small to moderate extent of melting of lithology B (*e.g.* short melting columns with $F_B < 16\%$), REE patterns in interstitial melts and mixed-column melts are sensitive to the fractions of Cpx and Opx in the pyroxenite. The greater the Opx to Cpx ratio in the pyroxenite, the smaller the bulk REE partition coefficients and the higher the REE concentrations in the melt will be. At a greater

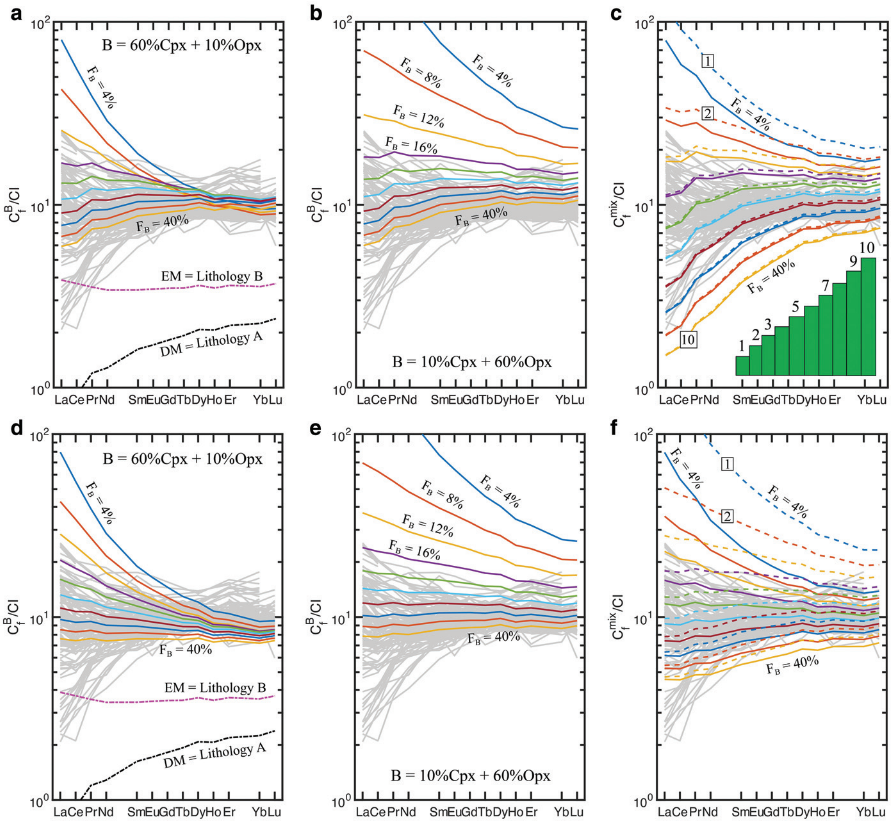

Fig. 6. Chondrite-normalized REE patterns in interstitial melts in lithology B (panels ***a, b, d, e***) and mixed-column melts (panels ***c, f***) produced by melting two peridotite-pyroxenite mantle sources. REE patterns in interstitial melts in lithology A are the same as those shown in Fig. 4a. Mantle source for lithology A is lherzolite (15% Cpx + 28% Opx + 57% olivine). Mantle source for lithology B is pyroxenite with either 60% Cpx + 10% Opx + 30% olivine (panels ***a, d***, and solid lines in ***c, f***) or 10% Cpx + 60% Opx + 30% Olivine (panels ***b, e***, and dashed lines in ***c, f***). Volume fractions of pyroxenite in the mantle source (ψ_B) are 10% for results presented in the first row (***a-c***) and 40% for results in the second row (***d-f***). The composition of lithology A is DMM of Workman and Hart (2005). The composition of lithology B is from the present author (dashed magenta lines in ***a*** and ***d***). Melting parameters are $\mathbb{R} = 1$ and $F_A^d = 4\%$. The maximum extent of melting for lithology A is 20% and the maximum extent of melting for lithology B is 40%. Other parameters and legends are the same as those used to construct Fig. 4.

extent of melting ($F_B > 16\%$), almost all REE in lithology B are partitioned into the melt. Consequently, REE patterns in the interstitial melt and the mixed-column melt are practically independent of melting parameters ($\mathbb{R}$ and F_A^d) and the relative proportion of Opx and Cpx in the pyroxenite (cf. dashed and solid lines of the same colour in Fig. 6c). Figure 6c shows that the LREE depleted patterns of the mixed-column melt are very similar to those produced by decompression melting of the homogeneous lherzolite with channelized melt migration in the dunite (cf. Figs 4c and 6c). Hence it is difficult to resolve contributions of the enriched mantle component based on REE patterns in D-MORB and N-MORB when the volume fraction of the enriched mantle is small in the mantle source. However, we may be able to tell such contributions from Sr-Nd-Hf-Pb isotope ratios in the samples. Such samples would be depleted in LREE but variously enriched in radiogenic isotope ratios.

When the volume fraction of the enriched mantle is large in the mantle source, it is possible to produce flat to LREE-enriched patterns in high-degree melts. Figure 6d–f provides one such example in which the volume fraction of pyroxenite is 40% in the mantle source. Other parameters are the same as those for Fig. 6a–c. Figure 7a–c further expands this case by reversing melt flow direction in the upper part of the melting column, *i.e.* from the pyroxenite (lithology A) to the lherzolite (lithology B). The LREE-depleted pattern in small-degree melts in the lherzolite ($F_B \leq 4\%$ in Fig. 7b) is produced by batch melting in the lower fifth of the melting column where no melt flows from the pyroxenite to the lherzolite. The flat to enriched LREE patterns in the mixed-column melts (Fig. 7c) are produced by a combination of fluxed batch melting in the lherzolite and near fractional melting in the LREE-enriched pyroxenite where part of the enriched melts are sucked into the lherzolite.

The preceding examples (Figs 4, 6, 7) demonstrate that a range of REE patterns for the mixed-column melt can be produced by decompression melting of a two-lithology mantle. These REE patterns are broadly similar to those observed in MORB. Similarities in REE patterns between the mixed-column melt and MORB suggest that the eruptible melt sampled on the surface or seafloor is not well mixed across the melting region.

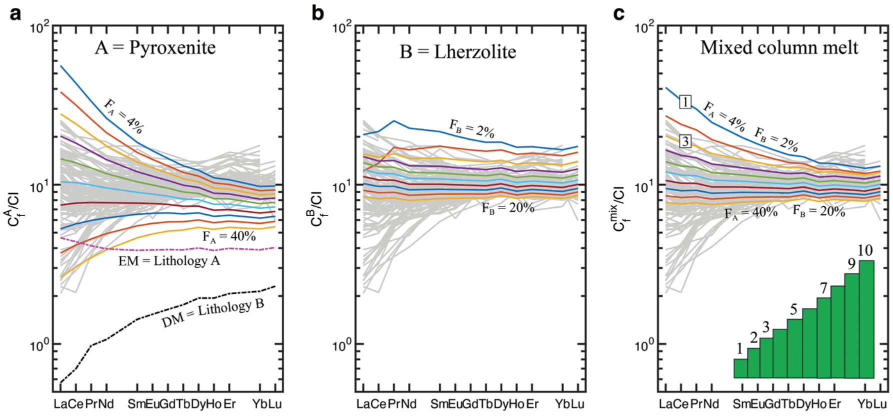

Fig. 7. Chondrite-normalized REE patterns in interstitial melts (***a, b***) and mixed-column melts (***c***) produced by decompression melting of a two-lithology mantle in which lithology A is pyroxenite (60% Cpx + 10% Opx + 30% olivine, 40% by volume) and lithology B is lherzolite (15% Cpx + 28% Opx + 57% olivine, 60% by volume). Part of the melt produced in the pyroxenite is sucked into the lherzolite ($\mathbb{R} = 1$ and $F_A^d = 8\%$). The maximum extent of melting for lithology A is 40% and the maximum extent of melting for lithology B is 20%. Other parameters and legends are the same as those used to construct Fig. 6d–f.

Incomplete mixing of different column melts at the top of the melting region (Fig. 1a) is a complicated process and will be the subject of future investigation.

8. Summary and discussion

Decompression melting is a dynamic process in which melt and solid flow at different rates and different directions. Locations and flow rates of the melt and residual solid in the melting column can be tracked using conservation equations. In this chapter, we present a set of steady-state melting models for decompression melting of a two-lithology mantle in which the enriched mantle is in the form of long strings (Fig. 1a). We show that the widely used simple melting models can be obtained by solving a set of conservation equations under nearly identical setups (Fig. 1b). Melt and solid mass fluxes have played a central role in quantifying trace element concentrations. Different melting models have different melt fluxes. Batch melting, fractional melting, continuous melting and two-porosity melting models can be unified through the two-lithology melting model (Eqs 49a–g, 8–9, Fig. 2). The melt suction rate is a key parameter determining the style of melting in lithology A. It is shown here that melting in lithology B is characterized by fluxed batch melting (Eqs 49c–e) so long as melt flows from lithology A into lithology B. Melting in lithology A can be interpreted as a ‘defluxed’ batch melting (Eq. 33c) as long as melt flows out of lithology A. For modelling trace element fractionation during decompression melting of a heterogeneous mantle, we recommend the two-lithology melting model.

We demonstrate the usefulness of the conserved form of mass conservation equations in finding simple solutions for concentrations of the average melt and mixed-column melt at top of the melting column. The eruptible melt is formed by incomplete mixing of mixed-column melts from several melting columns across the melting region. However, the process of mixing is still not well understood and requires further study. Our formulations for the average melt (Eq. 1), eruptible melt (Eq. 2) and mixed-column melt compositions (Eqs 8–9) are general and can also be used for modelling major elements. For highly incompatible trace elements, we show that mixing of melts from the enriched and depleted lithologies at top of the melting column is equivalent to mixing of the two sources weighted by the fraction of melts produced in the two-lithology column (Eq. 10a). In terms of ratios of isotopes or highly incompatible trace elements, mixing of melts from the two lithologies at top of the melting column is equivalent to mixing of the two sources (Eq. 10b).

Through applications of mass conservation equations, we have gained a better understanding of the widely used continuous or dynamic melting model. Contrary to constant porosity assumption that underpins the original development of the continuous melting model, porosity decreases upwards in the upper part of the melting column during continuous melting in an upwelling column (Fig. 3b). This happens because the solid mass flux decreases upwards in the melting column. To maintain the original mathematical form for continuous melting, the melt-to-solid mass flux ratio must remain constant and uniform in the upper part of melting column. Constant and uniform porosity is established when the amount of melt produced is balanced by the amount of melt extracted in the melting column. This is the case of constant melt flux model which has a slightly different form than the continuous melting model. When the extent of melting experienced by lithology A is not large (<20%), the differences between the two cases are small in terms of concentration and porosity. Irrespective of the choice of melt flux in the continuous melting model, porosity in lithology B always increases upwards in the melting column (Eqs 53a and 53b).

The two-lithology melting model also has two porosities (Fig. 3c). We show that high-porosity channels form naturally during decompression melting in a two-lithology mantle when melt produced in one lithology flows into another lithology and the melting rates of the two lithologies are different. The formation of dunite channels has a dilution effect on incompatible trace element concentrations in the channel melt (Eqs 50–51), which may provide a simple mechanism for producing highly depleted melts, such as those found in some olivine-hosted melt inclusions. In the presence of an enriched mantle source, the dilution effect may be obscured. It is possible to produce melts with depleted incompatible trace elements patterns but isotopically enriched signals.

We show through simple examples that it is possible to produce partial and well-mixed melts with a range of REE patterns by decompression melting of a two-lithology mantle, from LREE depleted to LREE enriched, similar to those observed in MORB. We have reasonably good knowledge of the composition and melting parameters of the depleted mantle source (*i.e.* its lithology, melting reaction and mineral-melt trace element partition coefficients). However, such knowledge is incomplete for the enriched mantle and requires further studies.

Although the steady-state melting models presented in this study are derived under the simplification of constant melting rate, the solutions remain valid when the melting rate varies spatially in the melting column. The degree of melting is related to the variable melting rate through the integral in Eq. 16. The melt suction rate in the four models presented here takes on one or two constant values in the melting column. This allows us to obtain simple analytical solutions for the melting problems. In a more general case, the melt suction rate varies continuously along the melting column, starting from zero at the solidus. Melt may flow from lithology A to lithology B in one part of the melting column but reverse its direction in another part of the melting column. The latter may serve as a mechanism for mantle metasomatism. Part of lithology A may transform into lithology B or vice versa. Liang and Parmentier (2010) presented some numerical examples of these more general cases. Dygert *et al.* (2016) presented a field example of infiltration of dunite-hosted melts into the host harzburgite and lherzolite from the Trinity ophiolite.

Finally, the two-lithology models presented here are independent of time. They are developed under the assumption that the shape of lithology B is a long string, interconnected in the vertical direction (Fig. 1). When the size of lithology B is smaller than the height of the melting column, different parcels of lithology B enter the melting column at different times. The melting problem becomes time dependent. Liang (2008) and Liang and Liu (2018) presented time-dependent solutions for batch melting, fractional melting, continuous melting and two-porosity melting of a heterogeneous mantle column in which the enriched and depleted mantle sources have the same lithology and melting rate (*i.e.* a chemically heterogeneous mantle). Liang (2020, 2022) further expanded the perfect fractional melting model by allowing the depleted and enriched mantle sources to have different melting rate and partition coefficient (*i.e.* a lithologically heterogeneous mantle). However, explicit expressions for a more general time-dependent model in which melt percolates in the two lithologies still awaits further development (for a preview see supplementary Movie_4 in Liang, 2020).

Acknowledgements

I thank Romain Tilhac and Alessio Sanfilippo for constructive reviews that greatly improved the presentation of this manuscript. Nick Dygert, Noah Hooper, Boda Liu and Chenguang Sun read earlier versions of this manuscript and made many useful suggestions. I would also like to thank Boda Liu, Marc Parmentier and Chenguang Sun for fruitful collaborations and stimulating discussions on trace element partitioning, channelized melt migration and decompression mantle melting. Some of the materials presented here are based on lecture notes used in a Geochemical Modelling course taught by the author at Brown University. I thank participating students for their interest and contributions. Work on mantle melting and trace element fractionation at Brown University has been supported by NSF and NASA, mostly recently through grants OCE-1852088, EAR-2147598 and 80NSSC22K0975.

Appendix A. Conservation equations for lithology A

The one-dimensional mass-conservation equations for interstitial melt and residual solid in the upwelling melting column are:

$$\frac{\partial \rho_f \phi_f^A \psi_A}{\partial t} + \frac{\partial \rho_f \phi_f^A V_f^A \psi_A}{\partial z} = \psi_A \Gamma_A - \dot{S} \tag{A1}$$

$$\frac{\partial \rho_s \left(1 - \phi_f^A\right) \psi_A}{\partial t} + \frac{\partial \rho_s \left(1 - \phi_f^A\right) V_s^A \psi_A}{\partial z} = -\psi_A \Gamma_A \tag{A2}$$

where t is time; z is the vertical coordinate, positive upwards; ρ_f and ρ_s are densities of the melt and solid, respectively; ϕ_f^A and V_f^A are the porosity (volume fraction) and velocity of interstitial melt of lithology A in the melting column, respectively; V_s^A is the solid velocity; and $\dot{S}$ is the melt suction rate (amount of melt flowing from lithology A to lithology B per unit volume of the two lithology per unit time). The mass conservation equation for a trace element in the bulk lithology A (melt + solid) is:

$$\frac{\partial \left[\rho_f \phi_f^A C_f^A + \rho_s \left(1 - \phi_f^A\right) C_s^A\right] \psi_A}{\partial t} + \frac{\partial \left[\rho_f \phi_f^A V_f^A C_f^A + \rho_s \left(1 - \phi_f^A\right) V_s^A C_s^A\right] \psi_A}{\partial z} = -\dot{S} C_f^A \tag{A3}$$

where C_f^A and C_s^A are concentrations of the trace element in the interstitial melt and residual solid in lithology A, respectively. Equation A3 states that the rate of change of total concentration of the trace element in lithology A in a representative element volume (REV) at location z in the melting column is due to flow of the melt and solid across the REV (second term on the left-hand-side) and transfer of the trace element in the melt from lithology A to lithology B (the term on the right-hand side). At steady state, these two terms balance with each other. When the solid and melt are in local chemical equilibrium, Eq. A3 can be simplified through the bulk solid-melt partition coefficient, *i.e.* $C_s^A = k_A C_f^A$. We have:

$$\frac{\partial\left[\rho_f \phi_f^A + \rho_s\left(1-\phi_f^A\right)k_A\right]\psi_A C_f^A}{\partial t} + \frac{\partial\left[\rho_f \phi_f^A V_f^A + \rho_s\left(1-\phi_f^A\right)V_s^A k_A\right]\psi_A C_f^A}{\partial z} = -\dot{S}C_f^A \tag{A4}$$

With the help of Eqs A1, A2 and A7 below, Eq. A4 can be further simplified:

$$\frac{\partial\left[\rho_f \phi_f^A + \rho_s\left(1-\phi_f^A\right)k_A\right]C_f^A}{\partial t} + \left[\rho_f \phi_f^A V_f^A + \rho_s\left(1-\phi_f^A\right)V_s^A k_A\right]\frac{\partial C_f^A}{\partial z} = \left(k_A^p - 1\right)C_f^A \Gamma_A \tag{A5}$$

We refer to Eqs A3 and A4 as the conserved form and to Eq. A5 as the non-conserved form. As shown in the main text, the conserved form is useful to calculate concentration of the aggregated or pooled melt at top of the melting column, whereas the non-conserved form is more convenient to calculate concentration of instantaneous melt in the melting column. To solve Eq. A4 or A5, we also need know the bulk partition coefficient and the extend of melting experienced by residual solid at a given time and location in the melting column. These melting parameters are defined with respect to the upwelling solid by the following evolution equations:

$$\frac{\partial F_A}{\partial t} + V_s^A \frac{\partial F_A}{\partial z} = \frac{(1-F_A)\Gamma_A}{\rho_s\left(1-\phi_f^A\right)} \tag{A6}$$

$$\frac{\partial k_A}{\partial t} + V_s^A \frac{\partial k_A}{\partial z} = \frac{\left(k_A - k_A^p\right)\Gamma_A}{\rho_s\left(1-\phi_f^A\right)} \tag{A7}$$

The factor 1 – F_A in Eq. A6 accounts for the fact that the F_A fraction of fusible solid has already been converted to melt at location z in the melting column at time t. The difference in partition coefficient in Eq. A7 arises from non-modal melting. The left-hand side of Eqs A6 and A7 are material derivatives following the motion of solid.

The bulk solid-melt partition coefficient (k_A) and the partition coefficient according to melting reaction (k_A^p) for a trace element are defined in the usual way (Shaw, 1970):

$$k_A = \sum_{j=1}^{N} w_j^A k_j^A \tag{A8}$$

$$k_A^p = \sum_{j=1}^{N} p_j^A k_j^A \tag{A9}$$

where w_j^A is the weight fraction of mineral j in the solid; p_j^A is the fraction of mineral j participated in the melting reaction; and k_j^A is the mineral-melt partition coefficient for mineral j. The bulk solid-melt partition coefficient k_A depends on mineral mode, while k_A^p depends on the melting reaction. Hence both partition coefficients are lithology specific. Derivations of the conservation and evolution equations outline in Appendices A and B can be found in Liang and Parmentier (2010), Liang and Peng (2010) and Liang (2020).

Appendix B. Conservation equations for lithology B

Conservation and evolution equations for lithology B are similar to those for lithology A except we have to reverse the sign for the source term involving flow or suction of melt from lithology A to lithology B. These equations are:

$$\frac{\partial \rho_f \phi_f^B \psi_B}{\partial t} + \frac{\partial \rho_f \phi_f^B V_f^B \psi_B}{\partial z} = \psi_B \Gamma_B + \dot{S} \tag{B1}$$

$$\frac{\partial \rho_s \left(1 - \phi_f^B\right) \psi_B}{\partial t} + \frac{\partial \rho_s \left(1 - \phi_f^B\right) V_s^B \psi_B}{\partial z} = -\psi_B \Gamma_B \tag{B2}$$

$$\begin{aligned}&\frac{\partial \left[\rho_f \phi_f^B C_f^B + \rho_s \left(1 - \phi_f^B\right) C_s^B\right] \psi_B}{\partial t} + \frac{\partial \left[\rho_f \phi_f^B V_f^B C_f^B + \rho_s \left(1 - \phi_f^B\right) V_s^B C_s^B\right] \psi_B}{\partial z} \\ &= \dot{S} C_f^A\end{aligned} \tag{B3}$$

Note the solid velocity for lithology B may not be the same as that for lithology A. When the solid and melt are in local chemical equilibrium, we have the conserved form of mass conservation equation for a trace element in lithology B:

$$\frac{\partial\left[\rho_f\phi_f^B+\rho_s\left(1-\phi_f^B\right)k_B\right]\psi_B C_f^B}{\partial t}+\frac{\partial\left[\rho_f\phi_f^B V_f^B+\rho_s\left(1-\phi_f^B\right)V_s^B k_B\right]\psi_B C_f^B}{\partial z}$$
$$=\dot{S}C_f^A \tag{B4}$$

The non-conserved form of Eq. B4 is:

$$\frac{\partial\left[\rho_f\phi_f^B+\rho_s\left(1-\phi_f^B\right)k_B\right]C_f^B}{\partial t}+\left[\rho_f\phi_f^B V_f^B+\rho_s\left(1-\phi_f^B\right)V_s^B k_B\right]\frac{\partial C_f^B}{\partial z}$$
$$=\left(k_B^p-1\right)C_f^B\Gamma_B+\dot{S}\left(C_f^A-C_f^B\right) \tag{B5}$$

The last term on the right-hand side of Eq. B5 accounts for the flow of melt from lithology A to lithology B. Evolution equations for the extent of melting and bulk partition coefficient are:

$$\frac{\partial F_B}{\partial t}+V_s^B\frac{\partial F_B}{\partial z}=\frac{(1-F_B)\Gamma_B}{\rho_s\left(1-\phi_f^B\right)} \tag{B6}$$

$$\frac{\partial k_B}{\partial t}+V_s^B\frac{\partial k_B}{\partial z}=\frac{\Gamma_B\left(k_B-k_B^p\right)}{\rho_s\left(1-\phi_f^B\right)} \tag{B7}$$

The bulk partition coefficient (k_B) and the partition coefficient according to the melting reaction (k_B^p) for lithology B are defined in a similar way as those in Eqs A8 and A9, *i.e.*

$$k_B=\sum_{j=1}^{N}w_j^B k_j^B \tag{B8}$$

$$k_B^p=\sum_{j=1}^{N}p_j^B k_j^B \tag{B9}$$

Appendix C. Mixed-column melt composition

At the top of the melting column, melts derived from lithology A and lithology B mix in accordance with their mass fluxes. The composition of the well-mixed melt at top of the melting column (C_f^{mix}) is the weighted average:

$$C_f^{mix} = \frac{\rho_f \phi_f^A V_f^A \psi_A C_f^A + \rho_f \phi_f^B V_f^B \psi_B C_f^B}{\rho_f \phi_f^A V_f^A \psi_A + \rho_f \phi_f^B V_f^B \psi_B} \tag{C1}$$

The denominator in Eq. C1 is the total melt flux at top of the melting column which can also be written as:

$$\rho_f \phi_f^A V_f^A \psi_A + \rho_f \phi_f^B V_f^B \psi_B = \rho_s V_s^0 F_A \psi_A + \rho_s V_s^0 F_B \psi_B \tag{C2}$$

The numerator in Eq. C1 can be evaluated by summing the steady-state version of Eqs A3 and B3:

$$\frac{d\left[\rho_f \phi_f^A V_f^A C_f^A + \rho_s\left(1 - \phi_f^A\right) V_s^A C_s^A\right]\psi_A}{dz} + \frac{\partial\left[\rho_f \phi_f^B V_f^B C_f^B + \rho_s\left(1 - \phi_f^B\right) V_s^B C_s^B\right]\psi_B}{dz} = 0 \tag{C3}$$

Integrating Eq. C3 from the solidus to the top of the melting column, we have

$$\rho_f \phi_f^A V_f^A C_f^A \psi_A + \rho_f \phi_f^B V_f^B C_f^B \psi_B = \left[\rho_s V_s^0 C_A^0 - \rho_s\left(1 - \phi_f^A\right) V_s^A C_s^A\right]\psi_A + \left[\rho_s V_s^0 C_B^0 - \rho_s\left(1 - \phi_f^B\right) V_s^B C_s^B\right]\psi_B \tag{C4}$$

Equation C4 states that the total mass flux of the element of interest available for melt extraction (the left-hand side) is the net difference between the total mass flux of the mantle source materials feeding into the melting column from below and the total mass flux of the residual solid left behind at top of the melting column. This statement is independent of melting models and how lithology A and lithology B interact in the melting column. Hence Eq. C4 is a general statement of steady-state global mass balance in the two-lithology melting column. In terms of the degree of melting, Eq. C4 takes the form:

$$\rho_f \phi_f^A V_f^A C_f^A \psi_A + \rho_f \phi_f^B V_f^B C_f^B \psi_B = \rho_s V_s^0 \left\{\left[C_A^0 - (1 - F_A) C_s^A\right]\psi_A + \left[C_B^0 - (1 - F_B) C_s^B\right]\psi_B\right\} \tag{C5}$$

Substituting Eq. C5 into Eq. C1, we have a simple expression for the concentration of well-mixed melt at top of the two-lithology melting column:

$$C_f^{mix} = \frac{\psi_A\left[C_A^0 - (1 - F_A) C_s^A\right] + \psi_B\left[C_B^0 - (1 - F_B) C_s^B\right]}{\psi_A F_A + \psi_B F_B} \tag{C6}$$

In terms of instantaneous melt composition, Eq. C6 can be written as:

$$C_f^{mix} = \frac{\psi_A\left[C_A^0 - (1 - F_A)k_A C_f^A\right] + \psi_B\left[C_B^0 - (1 - F_B)k_B C_f^B\right]}{\psi_A F_A + \psi_B F_B} \qquad \text{(C7a)}$$

For non-modal melting, we have:

$$C_f^{mix} = \frac{\psi_A\left[C_A^0 - \left(k_A^0 - k_A^p F_A\right)C_f^A\right] + \psi_B\left[C_B^0 - \left(k_B^0 - k_B^p F_B\right)C_f^B\right]}{\psi_A F_A + \psi_B F_B} \qquad \text{(C7b)}$$

Equations C6–C7 are mixing models for modelling major and trace element variations during decompression melting of a steady-state two-lithology melting column. To calculate the concentration of the element of interest in the well-mixed melt at top of the melting column, we need to know volume proportions of the two lithologies in the mantle source, extents of melting experienced by the two lithologies at top of the melting column and concentrations of the melt or residual solid in the two lithologies at top of the melting column. These equations can be generalized to an N-lithology mantle source:

$$C_f^{mix} = \frac{\sum_{j=1}^{N} \psi_j\left[C_j^0 - \left(1 - F_j\right)C_s^j\right]}{\sum_{j=1}^{N} \psi_j F_j} \qquad \text{(C8a)}$$

$$C_f^{mix} = \frac{\sum_{j=1}^{N} \psi_j\left[C_j^0 - \left(1 - F_j\right)k_j C_f^j\right]}{\sum_{j=1}^{N} \psi_j F_j} \qquad \text{(C8b)}$$

where index j refers to properties of lithology j.

Appendix D. Porosity in the melting column

Porosity in the melting column depends on melt flux which in turn depends on the melt suction rate. To demonstrate the basic idea, here we ignore compaction in the melting column and use Darcy's law to estimate melt porosity in the two-lithology melting column. The procedure is the same as that outlined by Liang and Liu (2018) for decompression melting for a constant and uniform melt suction rate. Including solid upwelling, Darcy's law for the two lithologies are (McKenzie, 1984):

$$\phi_f^A\left(V_f^A - V_s^A\right) = \frac{\kappa_\phi^A}{\eta_f}\left(1 - \phi_f^A\right)\Delta\rho g \tag{D1a}$$

$$\phi_f^B\left(V_f^B - V_s^B\right) = \frac{\kappa_\phi^B}{\eta_f}\left(1 - \phi_f^B\right)\Delta\rho g \tag{D1b}$$

where κ_ϕ^A and κ_ϕ^B are permeabilities of lithologies A and B in the melting column; η_f is the melt viscosity; $\Delta\rho = \rho_s - \rho_f$; and g is the acceleration due to gravity. With the help of Eqs 47 and 49f, we write the relative volume flux of the melt in Eq. D1 as

$$\phi_f^A\left(V_f^A - V_s^A\right) = V_s^0\left[(1 - \mathbb{R})F_A + \mathbb{R}F_A^d - \phi_f^A(1 - F_A)\right] \tag{D2a}$$

$$\phi_f^B\left(V_f^B - V_s^B\right) = V_s^0\left[F_B + \mathbb{R}\left(F_A - F_A^d\right)\frac{\psi_A}{\psi_B} - \phi_f^B(1 - F_B)\right] \tag{D2a}$$

where we make use of the simplifications: $\phi_f^A \ll 1$, $\phi_f^B \ll 1$ and $\rho_s/\rho_f \to 1$. The permeability is related to porosity and mean grain size (d_A, d_B) through the power-law relationships:

$$\kappa_\phi^A = \frac{d_A^2}{b}\left(\phi_f^A\right)^n, \quad \kappa_\phi^B = \frac{d_B^2}{b}\left(\phi_f^B\right)^n \tag{D3a, D3b}$$

where n is the permeability exponent; and b is a constant. For the case presented in section 5, we set $n = 3$ based on the study of Wark and Watson (1998). Substituting Eqs D2 and D3 into Darcy's law, we have a set of algebraic equations for porosities in the two lithologies:

$$\left(\phi_f^A\right)^n = \frac{b\eta_f}{d_A^2\Delta\rho g}V_s^0\left[(1 - \mathbb{R})F_A + \mathbb{R}F_A^d - \phi_f^A(1 - F_A)\right] \tag{D4a}$$

$$\left(\phi_f^B\right)^n = \frac{b\eta_f}{d_B^2\Delta\rho g}V_s^0\left[F_B + \mathbb{R}\left(F_A - F_A^d\right)\frac{\psi_A}{\psi_B} - \phi_f^B(1 - F_B)\right] \tag{D4b}$$

It is convenient to introduce two reference porosities in terms of the maximum extents of melting experienced by the two lithologies in the melting column:

$$\phi_{ref}^A = \left(\frac{b\eta_f}{d_A^2\Delta\rho g}V_s^0 F_A^{\max}\right)^{\frac{1}{n}}, \quad \phi_{ref}^B = \left(\frac{b\eta_f}{d_B^2\Delta\rho g}V_s^0 F_B^{\max}\right)^{\frac{1}{n}} \tag{D5a, D5b}$$

Equations D4a–D4b then take on the forms:

$$\left(\phi_f^A\right)^n = \frac{\left(\phi_{ref}^A\right)^n}{F_A^{\max}}\left[(1-\mathbb{R})F_A + \mathbb{R}F_A^d - \phi_f^A(1-F_A)\right] \tag{D6a}$$

$$\left(\phi_f^B\right)^n = \frac{\left(\phi_{ref}^B\right)^n}{\psi_B F_B^{\max}}\left[\psi_B F_B + \psi_A \mathbb{R}\left(F_A - F_A^d\right) - \psi_B \phi_f^B(1-F_B)\right] \tag{D6b}$$

Given the reference porosity and melting parameters, Eq. D6 can be solved ‘exactly’ using a numerical method. An approximate solution to Eqs D6a–D6b can be obtained by ignoring the third term in the square bracket on the right-hand side of these equations, *i.e.*

$$\phi_f^A \approx \phi_{ref}^A\left[\frac{(1-\mathbb{R})F_A + \mathbb{R}F_A^d}{F_A^{\max}}\right]^{\frac{1}{n}} \tag{D7a}$$

$$\phi_f^B \approx \phi_{ref}^B\left[\frac{\psi_B F_B + \psi_A \mathbb{R}\left(F_A - F_A^d\right)}{\psi_B F_B^{\max}}\right]^{\frac{1}{n}} \tag{D7b}$$

When $F_A^d = 0$, Eq. D7a is reduced to the expression for constant and uniform melt suction rate in the melting column (Liang and Liu, 2018), *i.e.*

$$\phi_f^A \approx \phi_{ref}^A\left[(1-\mathbb{R})\frac{F_A}{F_A^{\max}}\right]^{\frac{1}{n}} \tag{D8}$$

Porosity obtained from the approximate solutions (Eqs D7a and D7b) are slightly smaller than the ‘exact’ values given by Eq. D6a and D6b (by $<5\%$, relative).

Appendix E. Summary of melting models

To facilitate geochemical modelling, here we list key equations for the four melting models presented in sections 3–5. These equations are identified by their original equation numbers so a reader can easily find relevant information in the main text. Common to the four models are the dimensionless melt suction rate, bulk partition coefficient, extent of melting, equilibrium partitioning between residual solid and interstitial melt and expressions for aggregated melts.

- Dimensionless melt suction rate

$$\mathbb{R} = \frac{\dot{S}}{\psi_A \Gamma_A} \tag{17c}$$

- Degrees of melting for the two litholgies

$$F_A = \frac{\Gamma_A z}{\rho_s V_s^0}, \quad F_B = \frac{\Gamma_B z}{\rho_s V_s^0} \tag{16, 30c}$$

- Bulk solid-melt partition coefficients

$$k_A = \frac{k_A^0 - k_A^p F_A}{1 - F_A}, \quad k_B = \frac{k_B^0 - k_B^p F_B}{1 - F_B} \tag{19b, 30d}$$

- Concentrations of residual solid in lithologies A and B

$$C_s^A = k_A C_f^A, \quad C_s^B = k_B C_f^B \tag{23, 33b}$$

- Mixed-column melt at the top of the two-lithology melting column

In terms of interstitial melt composition:

$$C_f^{mix} = \frac{\psi_A F_A C_f^A + \psi_B F_B C_f^B}{\psi_A F_A + \psi_B F_B} \tag{8}$$

In terms of residual solid composition:

$$C_f^{mix} = \frac{\psi_A \left[C_A^0 - (1 - F_A) C_s^A \right] + \psi_B \left[C_B^0 - (1 - F_B) C_s^B \right]}{\psi_A F_A + \psi_B F_B} \tag{9a}$$

- Eruptible melt composition

$$C_f^{eruptible} = \alpha_1 C_{f,1}^{mix} + \alpha_2 C_{f,2}^{mix} + \ldots + \alpha_N C_{f,N}^{mix} \tag{2a}$$

$$\alpha_1 + \alpha_2 + \ldots + \alpha_N = 1 \quad \text{and} \quad 0 \le \alpha_j \le 1 \tag{2b}$$

- Average melt composition over the entire melting region

$$C_f^{avg} = \frac{\bar{F}_1 C_{f,1}^{mix} + \bar{F}_2 C_{f,2}^{mix} + \ldots + \bar{F}_N C_{f,N}^{mix}}{\bar{F}_1 + \bar{F}_2 + \ldots + \bar{F}_N} \tag{1a}$$

$$\bar{F}_j = \psi_{A,j} F_{A,j} + \psi_{B,j} F_{B,j} \tag{1b}$$

$$\psi_{A,j} + \psi_{B,j} = 1 \tag{1c}$$

E1. The two-porosity melting model: Case of one melt suction rate (section 3)

- Concentration of instantaneous melt in lithology A

$$C_f^A = \begin{cases} \dfrac{C_A^0}{k_A^0}\left[\dfrac{k_A^0 + \left(1 - k_A^p - \mathbb{R}\right)F_A}{k_A^0}\right]^{\dfrac{k_A^p - 1}{1 - k_A^p - \mathbb{R}}} & \text{if } 1 - k_m^p - \mathbb{R} \neq 0 \\ \dfrac{C_A^0}{k_A^0}\exp\left(\dfrac{k_A^p - 1}{k_A^0}F_A\right) & \text{if } 1 - k_m^p - \mathbb{R} = 0 \end{cases} \tag{21a, 21b}$$

- Average melt composition for lithology A

$$\bar{C}_f^A = \frac{C_A^0 - [(1 - \mathbb{R})F_A + (1 - F_A)k_A]C_f^A}{\mathbb{R}F_A} \tag{27b}$$

- Concentration of instantaneous melt in lithology B

$$C_f^B = \frac{\psi_B C_B^0 + \psi_A \mathbb{R} F_A \bar{C}_f^A}{\psi_B\left[k_B^0 + \left(1 - k_B^p\right)F_B\right] + \psi_A \mathbb{R} F_A} \tag{33a}$$

- Equations 21a and 21b reduce to batch melting when $\mathbb{R} = 0$ and fractional melting when $\mathbb{R} = 1$.

E2. The continuous melting model: Case of constant melt-to-solid mass flux (section 4.1)

- Concentration of instantaneous melt in lithology A

$$C_f^A = \frac{C_A^0}{k_A^0 + \left(1 - k_A^p\right)F_A} \quad \text{for } F_A < F_A^d \tag{38a}$$

$$C_f^A = \left[\frac{C_A^0}{k_A^0 + \left(1 - k_A^p\right)F_A^d}\right]\left[\frac{k_A^0 + \omega - \left(k_A^p + \omega\right)F_A}{k_A^0 + \omega - \left(k_A^p + \omega\right)F_A^d}\right]^{\dfrac{1 - k_A^p}{k_A^p + \omega}} \quad \text{for } F_A \geq F_A^d \tag{38b}$$

- Average melt composition for lithology A

$$\bar{C}_f^A = \frac{1}{F_A - F_A^d}\int_{F_A^d}^{F_A} C_f^A dF_A = \frac{C_A^0 - \left[k_A^0 + \omega - \left(k_A^p + \omega\right)F_A\right]C_f^A}{(1+\omega)\left(F_A - F_A^d\right)} \quad \text{for } F_A \geq F_A^d \tag{42c}$$

- Concentration of instantaneous melt in lithology B

$$C_f^B = \frac{C_B^0}{k_B^0 + \left(1 - k_B^p\right)F_B} \quad \text{for } F_A < F_A^d \tag{42a}$$

$$C_f^B = \frac{\psi_B C_B^0 + \psi_A(1+\omega)\left(F_A - F_A^d\right)\bar{C}_f^A}{\psi_B\left[k_B^0 + \left(1 - k_B^p\right)F_B\right] + \psi_A(1+\omega)\left(F_A - F_A^d\right)} \quad \text{for } F_A \geq F_A^d \tag{42b}$$

- Key melting parameters

$$F_A^d = \frac{\omega}{1+\omega} \tag{36b}$$

$$\omega = \frac{\rho_f \phi_f^A V_f^A}{\rho_s\left(1 - \phi_f^A\right)V_s^A} \quad \text{and} \quad F_A^d = \frac{\rho_f \phi_f^A V_f^A}{\rho_f \phi_f^A V_f^A + \rho_s\left(1 - \phi_f^A\right)V_s^A} \tag{40}$$

$$\mathbb{R} = \frac{\dot{S}}{\psi_A \Gamma_A} = \begin{cases} 0 & \text{for } F_A < F_A^d \\ 1+\omega & \text{for } F_A \geq F_A^d \end{cases} \tag{41}$$

E3. The continuous melting model: Case of constant porosity in lithology A (section 4.2)

- Concentration of instantaneous melt in lithology A

$$C_f^A = \frac{C_A^0}{k_A^0 + (1 - k_A^p)F_A} \quad \text{for } F_A < F_A^d \tag{45a}$$

$$C_f^A = \left[\frac{C_A^0}{k_A^0 + (1 - k_A^p)F_A^d}\right]\left[\frac{k_A^0 + F_A^d - k_A^p F_A}{k_A^0 + (1 - k_A^p)F_A^d}\right]^{\frac{1 - k_A^p}{k_A^p}} \quad \text{for } F_A \geq F_A^d \tag{45b}$$

- Average melt composition for lithology A

$$\bar{C}_f^A = \frac{1}{F_A - F_A^d}\int_{F_A^d}^{F_A} C_f^A \, dF_A = \frac{C_A^0 - \left(k_A^0 + F_A^d - k_A^p F_A\right)C_f^A}{F_A - F_A^d} \quad \text{for } F_A \geq F_A^d \tag{45e}$$

- Concentration of instantaneous melt in lithology B

$$C_f^B = \frac{C_B^0}{k_B^0 + (1 - k_B^p)F_B} \quad \text{for } F_A < F_A^d \tag{45c}$$

$$C_f^B = \frac{\psi_B C_B^0 + \psi_A\left(F_A - F_A^d\right)\bar{C}_f^A}{\psi_B\left[k_B^0 + (1 - k_B^p)F_B\right] + \psi_A\left(F_A - F_A^d\right)} \quad \text{for } F_A \geq F_A^d \tag{45d}$$

- Key melting parameter

$$\mathbb{R} = \frac{\dot{S}}{\psi_A \Gamma_A} = \begin{cases} 0 & \text{for } F_A < F_A^d \\ 1 & \text{for } F_A \geq F_A^d \end{cases} \tag{44}$$

E4. The two-lithology melting model (section 5)

- Concentration of instantaneous melt in lithology A

$$C_f^A = \frac{C_A^0}{k_A^0 + (1 - k_A^p)F_A} \quad \text{for } F_A < F_A^d \tag{49a}$$

$$C_f^A = \left[\frac{C_A^0}{k_A^0 + \left(1 - k_A^p\right)F_A^d}\right]\left[\frac{k_A^0 + F_A^d\mathbb{R} + \left(1 - k_A^p - \mathbb{R}\right)F_A}{k_A^0 + \left(1 - k_A^p\right)F_A^d}\right]^{\frac{k_A^p - 1}{1 - k_A^p - \mathbb{R}}} \quad \text{for } F_A \geq F_A^d \tag{49b}$$

- Average melt composition for lithology A

$$\bar{C}_f^A = \frac{1}{F_A - F_A^d}\int_{F_A^d}^{F_A} C_f^A dF_A = \frac{C_A^0 - \left[k_A^0 + \mathbb{R}F_A^d + \left(1 - k_A^p - \mathbb{R}\right)F_A\right]C_f^A}{\mathbb{R}\left(F_A - F_A^d\right)} \quad \text{for } F_A \geq F_A^d \tag{49e}$$

- Concentration of instantaneous melt in lithology B

$$C_f^B = \frac{C_B^0}{k_B^0 + \left(1 - k_B^p\right)F_B} \quad \text{for } F_A < F_A^d \tag{49c}$$

$$C_f^B = \frac{\psi_B C_B^0 + \psi_A\mathbb{R}\left(F_A - F_A^d\right)\bar{C}_f^A}{\psi_B\left[k_B^0 + \left(1 - k_B^p\right)F_B\right] + \psi_A\mathbb{R}\left(F_A - F_A^d\right)} \quad \text{for } F_A \geq F_A^d \tag{49d}$$

- Key melting parameter

$$0 \leq \mathbb{R} \leq \mathbb{R}_{\max}, \quad \mathbb{R}_{\max} = \frac{F_A^{\max}}{F_A^{\max} - F_A^d} \tag{48}$$

- Mass fluxes of the melt and solid in lithology A

$$\rho_f \phi_f^A V_f^A = \begin{cases} \rho_s V_s^0 F_A & \text{for } F_A < F_A^d \\ \rho_s V_s^0 (1 - \mathbb{R})F_A + \rho_s V_s^0 F_A^d \mathbb{R} & \text{for } F_A \geq F_A^d \end{cases} \tag{47}$$

$$\rho_s\left(1 - \phi_f^A\right)V_s^A = \rho_s V_s^0 (1 - F_A) \tag{17b}$$

- Mass fluxes of the melt and solid in lithology B

$$\rho_f \phi_f^B V_f^B \psi_B = \begin{cases} \rho_s V_s^0 F_B \psi_B & \text{for } F_A < F_A^d \\ \rho_s V_s^0 \left[F_B \psi_B + \mathbb{R}\left(F_A - F_A^d \right) \psi_A \right] & \text{for } F_A \geq F_A^d \end{cases} \tag{49f}$$

$$\rho_s \left(1 - \phi_f^B \right) V_s^B = \rho_s V_s^0 (1 - F_B) \tag{30b}$$

References

Albarède, F. (1995) *Introduction to Geochemical Modelling*. Cambridge University Press, New York.

Asimow, P.D. and Stolper, E.M. (1999) Steady-steady mantle-melt interactions in one dimension: I. Equilibrium transport and melt focusing. *Journal of Petrology*, **40**, 475–494.

Borghini, G. and Fumagalli, P. (2020) Melting relations of anhydrous olivine-free pyroxenite Px1 at 2 GPa. *European Journal of Mineralogy*, **32**, 251–264.

Borghini, G., Fumagalli, P. and Rampone, E. (2017) Partial melting of secondary pyroxenite at 1 and 1.5 GPa and its role in upwelling heterogeneous mantle. *Contributions to Mineralogy and Petrology*, **172**, 70.

Dasgupta, R., Hirschmann, M.M. and Stalker, K. (2006) Immiscible transition from carbonate-rich to silicate-rich melts in the 3 GPa melting interval of eclogite + CO_2 and genesis of silica-undersaturated ocean island lavas. *Journal of Petrology*, **47**, 647–671.

Dygert, N., Liang, Y. and Kelemen, P. (2016) Formation of plagioclase lherzolite and associate dunite-harzburgite-lherzolite sequences by multiple episodes of melt percolation and melt-rock reaction: An example from the Trinity ophiolite, California, USA. *Journal of Petrology*, **57**, 815–838.

Gast, P.W. (1968) Trace element fractionations and the origin of tholeiitic and alkaline magma types. *Geochimica et Cosmochimica Acta*, **32**, 1057–1086.

Hofmann, A.W. (1997) Mantle geochemistry: the message from oceanic volcanism. *Nature*, **385**, 219–229.

Hofmann, A.W. (2003) Sampling mantle heterogeneity through oceanic basalts: Isotopes and trace elements. In: *Treatise on Geochemistry: The Mantle and Core* 2nd Edition (ed. R. W. Carlson). Elsevier, New York, pp. 61–101.

Hewitt, I.J. and Fowler, A.C. (2008) Partial melting in an upwelling mantle column. *Proceedings of the Royal Society of London A: Mathematical, Physical and Engineering Sciences*, **464**, 2467–2491.

Ito, G. and Mahoney, J.J. (2005) Flow and melting of a heterogeneous mantle: 1. Method and importance to the geochemistry of ocean island and mid-ocean ridge basalts. *Earth and Planetary Science Letters*, **230**, 29–46.

Iwamori, H. (1994) ^{238}U-^{230}Th-^{226}Ra and ^{235}U-^{231}Pa disequilibra produced by mantle melting and porous and channel flows. *Earth and Planetary Science Letters*, **125**, 1–16.

Jull, M., Kelemen, P.B. and Sims, K. (2002) Consequences of diffuse and channeled porous melt migration on Uranium series disequilibra. *Geochimica et Cosmochimica Acta*, **66**, 4133–4148.

Kogiso, T., Hirschmann, M.M. and Pertermann, M. (2004) High-pressure partial melting of mafic lithologies in the mantle. *Journal of Petrology*, **45**, 2407–2422.

Lambart, S., Laporte, D., Provost, A. and Schiano, P. (2012) Fate of pyroxenite-derived melts in the peridotite mantle: Thermodynamic and experimental constraints. *Journal of Petrology*, **53**, 451–476.

Lambart, S., Baker, M.B. and Stolper, E.M. (2016) The role of pyroxenite in basalt genesis: melt-PX, a melting parameterization for mantle pyroxenites between 0.9 and 5 GPa. *Journal of Geophysical Research*, **121**, 5708–5735.

Langmuir, C. H., Bender, J F., Bence, A. E., Hanson, G. N. and Taylor, S. R. (1977) Petrogenesis of basalts from the FAMOUS area: Mid-Atlantic Ridge. *Earth and Planetary Science Letters*, **36**, 133–156.

Laubier, M., Gale, A. and Langmuir, C.H. (2012) Melting and crustal processes at the FAMOUS segment (Mid-Atlantic Ridge): New insights from olivine-hosted melt inclusions from multiple samples. *Journal of Petrology*, **53**, 665–698.

Liang, Y. (2008) Simple models for dynamic melting in an upwelling heterogeneous mantle column: Analytical solutions. *Geochimica et Cosmochimica Acta*, **72,** 3804–3821.

Liang, Y. (2020) Trace element fractionation and isotope ratio variation during melting of a spatially distributed and lithologically heterogenous mantle. *Earth and Planetary Science Letters*, **552**, 116594.

Liang, Y. (2022) Mixing loops, mixing envelopes, and scatter correlations among trace elements and isotope ratios produced by mixing of melts derived from a spatially heterogenous mantle. *Journal of Petrology*, **63**, 1–16.

Liang, Y. and Liu, B. (2018) Stretching chemical heterogeneity by melt migration in an upwelling mantle: An analysis based on time-dependent batch melting and fractional melting models. *Earth and Planetary Science Letters*, **498**, 275–287.

Liang, Y. and Parmentier, E.M. (2010) A Two-Porosity Double Lithology Model for Partial Melting, Melt Transport and Melt–rock Reaction in the Mantle: Mass Conservation Equations and Trace Element Transport. *Journal of Petrology*, **51**, 125–152.

Liang, Y. and Peng, Q. (2010) Non-modal melting in an upwelling mantle column: Steady-state models with applications to REE depletion in abyssal peridotites. *Geochimica et Cosmochimica Acta*, **74**, 321–339.

Liang, Y., Schiemenz, A., Hesse, M., Parmentier, E.M. and Hesthaven, J.S. (2010) High-porosity channels for melt migration in the mantle: Top is the dunite and bottom is the harzburgite and lherzolite. *Geophysical Research Letters*, **37**, L15306.

Liu, B. and Liang, Y. (2020) Importance of the size and distribution of chemical heterogeneities in the mantle source to the variations of isotope ratios and trace element abundances in mid-ocean ridge basalts. *Geochimica et Cosmochimica Acta*, **268**, 383–404.

Lo Cascio, M. (2008) Kinetics of partial melting and melt-rock reaction in the Earth's mantle. Ph.D. Thesis, Brown University, https://doi.org/10.7301/Z0SF2TK0.

Lundstrom, C.C. (2000) Models of U-series disequilibria generation in MORB: The effect of two scales of melt porosity. *Physics of the Earth and Planetary Interiors*, **121**, 189–204.

Mallik, A. and Dasgupta, R. (2012) Reaction between MORB-eclogite derived melts and fertile peridotite and generation of ocean island basalts. *Earth and Planetary Science Letters*, **329-330**, 97–108.

McKenzie, D. (1984) The generation and compaction of partially molten rocks. *Journal of Petrology*, **25**, 713–765.

McKenzie, D. (1985) ^{230}Th-^{238}U disequilibrium and the melting processes beneath ridge axes. *Earth and Planetary Science Letters*, **72**, 149–157.

Niu, Y., Regelous, M., Wendt, I.J., Batiza, R. and O'Hara, M.J. (2002) Geochemistry of near-EPR seamounts: importance of source *vs.* process and the origin of enriched mantle component. *Earth and Planetary Science Letters*, **199**, 327–345.

Ozawa, K. (2001) Mass balance equations for open magmatic systems: Trace element behavior and its application to open system melting in the upper mantle. *Journal of Geophysical Research*, **106**, 13,407–13,434.

Pertermann, M. and Hirschmann, M.M. (2003) Partial melting experiments on a MORB-like pyroxenite between 2 and 3 GPa: Constraints on the presence of pyroxenite in basalt source regions from solidus location and melting rate. *Journal of Geophysical Research*, **108**, 2125, doi: 10.1029/2000JB000118.

Ribe, N.M. (1985) The generation and composition of partial melting in the earth's mantle. *Earth and Planetary Science Letters*, **73**, 361–376.

Richter, F.M. (1986) Simple models for trace element fractionation during melt segregation. *Earth and Planetary Science Letters*, **77**, 333–344.

Rudge, J.F., Maclennan, J. and Stracke, A. (2013) The geochemical consequences of mixing melts from a heterogeneous mantle. *Geochimica et Cosmochimica Acta*, **114**, 112–143.

Salters, V.J.M. and Stracke, A. (2004) Composition of the depleted mantle. *Geochemistry*, *Geophysics*, *and Geosystems*, **5**, Q05B07, doi: 10.1029/2003GC000597.

Schiemenz A., Liang Y. and Parmentier, E.M. (2011) A high-order numerical study of reactive dissolution in an upwelling heterogeneous mantle: I. Channelization, channel lithology, and channel geometry. *Geophysics Journal International*, **186**, 641–664.

Shaw, D.M. (1970) Trace element fractionation during anatexis. *Geochimica et Cosmochimica Acta*, **34**, 237–243.

Shaw, D.M. (2000) Continuous (dynamic) melting theory revisited. *The Canadian Mineralogist*, **38**, 1041–1063.

Shaw, D.M. (2006) *Trace Elements in Magmas*. Cambridge University Press, New York.

Shimizu, K., Saal, A., Myers, C.E., Nagle, A.N., Hauri, E.H., Forsyth, D.W., Kemenetsky, V.S. and Niu, Y. (2016) Two-component mantle-mixing model for the generation of mid-ocean ridge basalts: Implications for the volatile content of the Pacific upper mantle. *Geochimica et Cosmochimica Acta*, **176**, 44–80.

Shimizu, N. (1998) The geochemistry of olivine-hosted melt inclusions in a FAMOUS basalt ALV519-4-1. *Physics of the Earth and Planetary Interiors*, **107**, 183–201.

Shorttle, O., Rudge, J.F., Maclennan, J. and Rubin, K.H. (2016) A statistical description of concurrent mixing and crystallization during MORB differentiation: Implications for trace element enrichment. *Journal of Petrology*, **57**, 2127–2162.

Sobolev, A.V. and Shimizu, N. (1993) Ultra-depleted primary melt included in an olivine from the Mid-Atlantic Ridge. *Nature*, **363**, 151–154.

Soderman, C.R., Shorttle, O., Matthews, S. and Williams, H.M. (2022) Global trends in novel stable isotopes in basalts: Theory and observations. *Geochimica et Cosmochimica Acta*, **318**, 388–414.

Sparks, D.W. and Parmentier, E.M. (1991) Melt extraction from the mantle beneath spreading centers. *Earth and Planetary Science Letters*, **105**, 368–377.

Spiegelman, M. and Elliot, T. (1993) Consequences of melt transport for Uranium series disequilibrium. *Earth and Planetary Science Letters*, **118**, 1–20.

Stracke, A. (2012) Earth's heterogeneous mantle: A product of convection-driven interaction between crust and mantle. *Chemical Geology*, **330-331**, 274–299.

Stracke, A., Bizimis, M. and Salters, V.J.M. (2003) Recycling oceanic crust: Quantitative constraints. *Geochemistry*, *Geophysics*, *and Geosystems*, **4**, 8003, doi: 10.1029/2001GC00022.

Stracke, A. and Bourdon, B. (2009) The importance of melt extraction for tracing mantle heterogeneity. *Geochimica et Cosmochimica Acta*, **73**, 218–238.

Sun, C. and Liang, Y. (2012) The distribution REE between clinopyroxene and basaltic melt along a mantle adiabat: effect of major element composition, water, and temperature. *Contributions to Mineralogy and Petrology*, **163**, 807–823.

Sun, C. and Liang, Y. (2013) The importance of crystal chemistry on REE partitioning between mantle minerals (garnet, clinopyroxene, orthopyroxene, and olivine) and basaltic melts. *Chemical Geology*, **358**, 23–36.

Turner, S.J., Langmuir, C.H., Dungan, M.A. and Escrig, S. (2017) The importance of mantle wedge heterogeneity to subduction zone magmatism and the origin of EM1. *Earth and Planetary Science Letters*, **472**, 216–228.

Vollmer, R. (1976) Rb-Sr and U-Th-Pb systematics of alkaline rocks: the alkaline rocks from Italy. *Geochimica et Cosmochimica Acta*, **40**, 283–295.

Walter, M. (2014) Melt extraction and compositional variability in mantle lithosphere. In: *Treatise on Geochemistry: The Mantle and Core* (editor: R. W. Carlson), 2nd Edition, Elsevier, New York, pp. 393–419.

Wang, C., Liang, Y., Xu, W. and Dygert, N. (2013) Effect of melt composition on basalt and peridotite interaction: Laboratory dissolution experiments with applications to mineral compositional variations in mantle xenoliths from the North China Craton. *Contributions to Mineralogy and Petrology*, **166**, 1469–1488.

Wang, C., Lo, Cascio, M., Liang, Y. and Xu, W. (2020) An experimental study of peridotite dissolution in eclogite-derived melts: Implications for styles of melt-rock interaction in lithospheric mantle beneath the North China Craton. *Geochimica et Cosmochimica Acta*, **278**, 157–176.

Wark, D.A. and Watson, B.E. (1998) Grain-scale permeability of texturally equilibrated, monomineralic rocks. *Earth and Planetary Science Letters*, **164**, 591–605.

Weavor, B.L. (1991) The origin of ocean island basalt end-member compositions: trace element and isotopic constraints. *Earth and Planetary Science Letters*, **104**, 381–397.

White, W.M. (2015) Isotopes, DUPAL, LLSVPs, and Anekantavada. *Chemical Geology*, **419**, 10–28.

Willbold, M. and Stracke, A. (2006) Trace element composition of mantle end-members: Implications for recycling of oceanic and upper and lower continental crust. *Geochemistry*, *Geophysics*, *Geosystems*, **7**, Q04004, doi: 10.1029/2005GC001005.

Workman, R.K. and Hart, S.R. (2005). Major and trace element composition of the depleted MORB mantle (DMM). *Earth and Planetary Science Letters*, **231**, 53–72.

Yao, L., Sun, C. and Liang, Y. (2012) A parameterized model for REE distribution between low-Ca pyroxene and basaltic melts with applications to REE partitioning in low-Ca pyroxene along a mantle adiabat and during pyroxenite-derived melt and peridotite interaction. *Contributions to Mineralogy and Petrology*, **164**, 261–280.

Yasuda, A., Fujii, T. and Kurita, K. (1994) Melting phase relations of an anhydrous mid-ocean ridge basalt from 3 to 20 GPa: Implications for the behavior of subducted oceanic crust in the mantle. *Journal of Geophysical Research*, **99**, 9401–9414.

Yaxley, G.M. and Green, D.H. (1998) Reactions between eclogite and peridotite: mantle refertilisation by subduction of oceanic crust. *Schweizerisches Mineralogisches Petrographisches Mitteilungen*, **78**, 243–255.

Zindler, A. and Hart, S. (1986) Chemical geodynamics. *Annual Reveiews in Earth and Planetary Science*, **14**, 493–571.

Zindler, A., Staudigel, H. and Batiza, R. (1984) Isotope and trace element geochemistry of young Pacific seamounts: implications for the scale of upper mantle heterogeneity. *Earth and Planetary Science Letters*, **70**, 175–195.

Zou, H. (1998) Trace element fractionation during modal and nonmodal dynamic melting and open-system melting: A mathematical treatment. *Geochimica et Cosmochimica Acta*, **62**, 1937-1945.

Zou, H. (2007) *Quantitative Geochemistry*. World Scientific.